CrossMark

Aquaplanet Models on Eccentric Orbits: Effects of the Rotation Rate on Observables

Arthur D. Adams[1] , William R. Boos[2,3] , and Eric T. Wolf[4]

[1] Department of Astronomy, Yale University, New Haven, CT 06520, USA; arthur.adams@yale.edu
[2] Department of Earth and Planetary Science, University of California, Berkeley, CA 94720, USA
[3] Climate and Ecosystem Sciences Division, Lawrence Berkeley National Laboratory, Berkeley, CA 94720, USA
[4] Laboratory for Atmospheric and Space Physics, Department of Atmospheric and Oceanic Sciences, University of Colorado, Boulder, CO 80309, USA

Abstract

Rotation and orbital eccentricity both strongly influence planetary climate. Eccentricities can often be measured for exoplanets, but rotation rates are currently difficult or impossible to constrain. Here we examine how the combined effects of rotation and eccentricity on observed emission from ocean-rich terrestrial planets can be used to infer their rotation rates in circumstances where their eccentricities are known. We employ an Earth climate model with no land and a slab ocean, and consider two eccentricities ($e = 0.3$ and 0.6) and two rotation rates: a fast Earth-like period of 24 hr, and a slower pseudo-synchronous period that generalizes spin synchronization for eccentric orbits. We adopt bandpasses of the Mid-Infrared Instrument on the *James Webb Space Telescope* as a template for future photometry. At $e = 0.3$ the rotation rates can be distinguished if the planet transits near periastron, because slow rotation produces a strong day–night contrast and thus an emission minimum during periastron. However, light curves behave similarly if the planet is eclipsed near periastron, as well as for either viewing geometry at $e = 0.6$. Rotation rates can nevertheless be distinguished using ratios of emission in different bands, one in the water vapor window with another in a region of strong water absorption. These ratios vary over an orbit by $\lesssim 0.1$ dex for Earth-like rotation, but by 0.3–0.5 dex for pseudo-synchronous rotation because of large day–night contrast in upper-tropospheric water. For planets with condensible atmospheric constituents in eccentric orbits, rotation regimes might thus be distinguished with infrared observations for a range of viewing geometries.

Key words: planets and satellites: atmospheres – planets and satellites: oceans – planets and satellites: terrestrial planets – radiative transfer – techniques: photometric

1. Introduction

The geometry of a planet's orbit and the rate of its rotation are both key to understanding spatial and temporal variations in the heating of its atmosphere by its host star. On Earth, the solar heating at a given position and time is dominated by the 24 hr day–night cycle from rotation, as well as the annual cycle in the orientation of the axial tilt with respect to the Sun–Earth line. These diurnal and annual cycles, with their significantly different timescales, operate largely independently of each other. Additionally, Earth's nearly circular orbit means that variations in the Earth–Sun distance are small; Earth's seasons are driven primarily by obliquity rather than eccentricity. Differences in orbital eccentricity, planetary rotation rate, and axial tilt can all have large consequences for atmospheric heating rates and planetary climate. Here we examine how rotation rate and orbital eccentricity control, via the global atmospheric circulation, the radiative properties of a planet's surface and atmosphere. By using detailed representations of the circulation and radiative transfer, we wish to explore whether the rough scale of rotation rate can be inferred from a limited set of observable features.

In order to extend our understanding of how planetary rotation and orbit drive periodicities in temperatures on other planets, we need to obtain observational constraints on actual rotation rates and orbits. In cases where exoplanets have been detected via both the radial velocity and transit methods, one can reliably constrain both the orbital periods and eccentricities to fairly high precision. However, very few observational constraints exist for the rotation rates of exoplanets, Earth-like or otherwise. From tidal arguments we expect Hot Jupiters with short orbital periods to undergo spin–orbit synchronization[5] on timescales shorter than the ages of the systems (Goldreich & Soter 1966; Showman & Guillot 2002). More recently, de Wit et al. (2016) and Lewis et al. (2017) used phase photometry to constrain the range of possible rotation periods for the highly eccentric giant planet HD 80606 b. No observational constraints yet exist for the rotation rate of Earth-sized exoplanets.

The rotation rate will set both the motion of the sub-stellar point on the planet's surface and the nature of the global atmospheric circulation that, in turn, controls planetary climate. Merlis & Schneider (2010) demonstrated that for Earth-like planets on circular orbits, Earth-like rotation periods will have larger latitudinal gradients in temperature away from the equator (see also Cullum et al. 2014). In contrast, when rotation is slow ($P_{\rm rot} \sim P_{\rm orb}$) the surface temperature should scale with the local instellation, peaking at or near the longitude of the sub-stellar point, with weaker equator-to-pole temperature differences. At the surface, the effect of rotation rate on temperature should also depend on the depth of the ocean mixed layer. Bolmont et al. (2016) explored a range of eccentricities for aquaplanet models and demonstrated that increasing the thermal inertia of the oceans damps changes in the climate more efficiently. Accordingly, faster rotation in their models reduces the sensitivity of the climate to the thermal inertia of the oceans.

---

[5] This term is often used interchangeably with tidal locking. They are equivalent for circular orbits, but a perpetual day-side scenario is not strictly possible for nonzero orbital eccentricities due to the non-constant rate of change in true anomaly over the orbit.

When planets on highly non-circular orbits are considered, we expect many of the general predictions based on the broad regimes of rotation rate for circular orbits to be extensible. In the limit of slow rotation, the pseudo-synchronous rotation (PSR) rate (Hut 1981) effectively approximates spin–orbit synchronization around the time of periastron, when stellar forcing is maximal. The physicality of this predicted rate relies on certain assumptions, including a constant tidal lag, and its applicability to terrestrial planets is still debated. Makarov & Efroimsky (2013) make the case that the only stable equilibrium states for terrestrial systems are spin–orbit resonances, for example the 3:2 spin–orbit resonance seen in Mercury. Acknowledging this, in the calculations performed herein we adopt pseudo-synchronization primarily as an example of a rotation rate that for most eccentricities will be much slower than an Earth-like rotation. In contrast, for a much faster rotation like Earth's, we expect that strong east–west winds induced by planetary rotation will homogenize temperatures in longitude on timescales shorter than the rate of change in instellation due to the eccentric orbit[6].

With current observational limitations in mind, here we seek to understand the time variation of surface and atmospheric temperatures on Earth-like planets with contrasting rotation rates and orbital shapes. Our goal is to determine whether the effects of rotation and orbit on incident radiation could induce a response that would lead to observable differences, thereby indirectly providing a method for estimating the rotation rate when only eccentricity is constrained a priori. In the scenarios explored here we assume zero obliquity; unlike Earth, the primary driver of seasonal variations will be eccentricity rather than axial tilt. To pursue our goal we adapt a class of 3D models, often referred to as general circulation models (GCMs), which are most often used to simulate Earth's atmosphere. These GCMs allow for analysis of the effects of various properties of the planetary system on the evolution of climate (e.g., O'Gorman & Schneider 2008; Wolf & Toon 2013, 2014, 2015). Such models have also been developed for other terrestrial planets in the solar system, particularly Venus and Mars (e.g., Rossow 1983; Barnes et al. 1993, 1996; Haberle et al. 1993; Barnes & Haberle 1996; Forget et al. 1999, 2013; Lebonnois et al. 2010; Zalucha et al. 2010), and have been used to explore large-scale atmospheric circulation under differences in atmospheric composition, rotation rate, and surface gravity.

Beyond the solar system, GCMs now have a considerable history of use for possible planetary scenarios in other stellar systems. Significant modifications have been undertaken by numerous groups to accommodate unfamiliar orbital and surface conditions. Joshi et al. (1997) present an early example of a GCM applied to a hypothetical extrasolar planet, exploring the consequences of putting an Earth-like planet on a short-period, spin-synchronous orbit around a late-type star. Following this, Merlis & Schneider (2010) used a GCM to model an "aquaplanet," an Earth-like planet with its entire surface covered by water, with results discussed above. Such works adopt the complex representations of physics operating below the GCM grid scale (e.g., precipitating atmospheric convection and radiative transfer), originally developed for Earth, to predict the behavior of exoplanet atmospheres.

Both Joshi et al. (1997) and Merlis & Schneider (2010) assume a stable ocean cover for their initial conditions. The validity of this assumption is studied explicitly through the definition and continual refinement of the habitable zone (HZ), which is the range of star–planet separations for which a planet with an Earth-like mass, radius, and atmospheric composition and surface pressure can plausibly support liquid water oceans on its surface. The foundational works for our current HZ definition rely primarily on a 1D radiative–convective climate model (Kasting et al. 1993; Kopparapu et al. 2013). These idealized 1D models make some assumptions most relevant for Earth, but subsequent efforts by a wide range of researchers have extended the range of theoretical habitability, in both model complexity and parameter space (see review by Ramirez 2018). Leconte et al. (2013) demonstrated that 3D modeling is necessary to account for large-scale contrasts in surface temperature due to inefficient or non-isotropic energy redistribution; these conditions expand the range of stellar fluxes where a runaway greenhouse effect may be prevented. Also using 3D modeling, Yang et al. (2013) showed that accounting for cloud distribution and dynamics further expanded the parameter space where climates could be habitable, particularly for slowly rotating planets. More recently, Way et al. (2018) explored the effects of ocean heat transport, which is known to be a significant mechanism for energy transport on Earth, for a range of rotation rates and stellar fluxes.

Most relevant to our study are works that explored effects of orbital eccentricity, such as the interplay of obliquity and eccentricity using climate models of intermediate complexity (Linsenmeier et al. 2015), and using GCMs to explore the possible limitations of assumptions for sustained ocean cover (Bolmont et al. 2016), as well as non-terrestrial atmospheric properties and stellar types (Shields et al. 2016). GCMs have also been used under similar water-rich conditions to study changes in stellar luminosity due to spectral types (Shields et al. 2013, 2014) or evolution (Wolf & Toon 2015), and the work of Ramirez & Kaltenegger (2016) complements this analysis with a combination of stellar and planetary mass-loss models, accounting for physical mechanisms that may be relevant for potentially habitable planets orbiting a variety of host stellar types. Taken together, these previous studies provide a wide range of theoretical predictions for the conditions governing the possible existence and persistence of liquid water oceans on terrestrial-size planets. While our purpose is not to make a critique or refinement of the currently defined HZ, and while we limit ourselves to a solar-type host star of constant luminosity, we introduce these studies here to place a precedent for the range of orbital configurations currently thought to support ocean-covered planets.

The two primary parameters we vary are orbital eccentricity and rotation period, both of which have undergone substantial study in recent literature, especially for close-in giant planets. A significant amount of work has been done to model the atmospheric response of highly eccentric Hot Jupiters, given their much more favorable observability when compared with planets on Earth-like orbits. Langton & Laughlin (2008) made foundational hydrodynamic simulations of the upper atmospheres of known Hot Jupiters with orbital eccentricities as high as $e = 0.93$ (HD 80606 b), and demonstrated that the intense stellar forcing during periastron passage was the primary driver of atmospheric dynamics. For a similar set of

---

[6] For a review of the circulation of Earth's atmosphere, see Schneider (2006). For a recent review of the circulation of tidally-locked planets, see Pierrehumbert & Hammond (2019).

eccentric planets, Cowan & Agol (2011) characterized the predicted phase variations from the orbital and viewing geometry and bulk atmospheric dynamics and radiative transfer, an analysis that was extended to predict thermal timescales for planets on Earth-like orbits in Cowan et al. (2012). Kataria et al. (2013) presented the first fully 3D simulations for eccentric Hot Jupiters, and incorporated both the mean-flux normalization and PSR assumptions that we adopt here. They found that both planets on eccentric orbits and those on circular orbits exhibit qualitatively similar atmospheric features, such as equatorial jets and day–night temperature differences. These features depend largely on the rotation rate, which sets the strength of the Coriolis forces. Furthermore, they demonstrated that the viewing geometry, in particular the longitude of periastron, has a major effect on the observed shape and offset of thermal phase variations.

While GCMs can be used to explore a range of interesting and hypothetical atmospheric dynamics that might occur on exoplanets, we would like to go beyond this to make testable predictions. Here we focus on predictions that might be verified through broadband photometry, which generally offers a greater photon count than spectroscopy and therefore is invaluable for studying small, warm-to-cool, and therefore faint exoplanets. Many giant planets on extremely short orbits have been observed indirectly via transits and secondary eclipses, and in some cases have been examined over significant fractions of their orbits (see recent reviews by Parmentier & Crossfield 2018 and Kreidberg 2018). While transit detections have substantially increased the population of known extrasolar planets, secondary eclipse measurements provide a complementary set of data that helps constrain major properties of planets' emissions. From the depth of a planet's eclipse we can infer the temperature of its illuminated hemisphere, which gives clues to the atmospheric conditions. A key instrument for observing secondary eclipses has been the *Spitzer Space Telescope*'s Infrared Array Camera (Werner et al. 2004), which has four photometric bands spanning 3.6–8.0 μm. The majority of *Spitzer* secondary eclipses and phase curves observed with *Spitzer* were made during the "warm *Spitzer*" phase, with only the 3.6 and 4.5 μm remaining operational; a summary of these measurements and references can be found in Adams & Laughlin (2018). In some opportune cases *Spitzer* has been able to observe planets over full orbits in some combination of these bands, providing a temporal connection between night-side observations of a planet in transit and day-side observations of it in eclipse.

Taking inspiration from these past analyses, as well as current observational techniques, here we generate predictions of eclipse depths and phase photometry from an exoplanet GCM. We begin by describing our assumptions for both orbital eccentricity and planetary rotation rate, along with relevant background, in Section 2. In Section 3 we describe the GCM we employ, and how we use it to simulate observable quantities. We present our results in Section 4, focusing on both the internal properties of the planetary atmospheres and the consequent observables.

2. Assumptions of Rotation and Orbit

2.1. Orbital Eccentricity

Numerous HZ planets are known to have nonzero orbital eccentricity (Adams & Kane 2016). The role of the Lidov–Kozai

mechanism (Kozai 1962; Lidov 1962) in increasing the orbital eccentricity of terrestrial planets is explored in Spiegel et al. (2010), and subsequently in works such as Georgakarakos et al. (2016), Way & Georgakarakos (2016), and Deitrick et al. (2018). The process allows for the existence of highly eccentric Earth-sized planets with neighboring giant planets; orbital resonances between the planets and their mutual proximities are the two critical components to the mechanism's efficiency (Murray & Dermott 1999).

Williams & Pollard (2002) argue that the installation time-averaged over an orbit is the primary determinant of whether liquid water can be sustained on a terrestrial planet's surface. For eccentric orbits the mean-flux approximation (MFA) fixes the time-averaged instellation over an orbit to that of a reference planet on a circular orbit. When comparing the flux F with that of Earth, as a function of the stellar luminosity $L_\star$, semimajor axis a, and eccentricity e,

$$\left\langle \frac{F}{F_\oplus} \right\rangle = \frac{L_\star/L_\odot}{(a/a_\oplus)^2 \sqrt{1 - e^2}} \qquad (1)$$

where the reference values for Earth are taken to be $F_\oplus = 1360 \, \mathrm{W \, m^{-2}}$, $L_\odot = 3.83 \times 10^{26}$ W, and $a_\oplus = 1$ au. Angle brackets denote a time average over an orbit. Barnes et al. (2008) use the conclusion of Williams & Pollard (2002) to define an "eccentric HZ" by scaling the semimajor axis a with eccentricity according to the MFA (Equation (1)). All models presented here have their semimajor orbital axes (and by extension their orbital periods) set according to this approximation. Table 1 lists these values for a range of eccentricities.

2.2. Rotation Rate

Analogous to the synchronous limit for circular orbits, Hut (1981) presents a limiting rotation rate based on a tidal evolution argument for binary systems with eccentric orbits. The PSR period is calculated from this pseudo-synchronous rate, and may be written in units of the orbital period as

$$\frac{P_{\mathrm{PSR}}}{P_{\mathrm{orb}}} = \frac{\left(1 + 3e^2 + \frac{3}{8}e^4\right)(1 - e^2)^{3/2}}{1 + \frac{15}{2}e^2 + \frac{45}{8}e^4 + \frac{5}{16}e^6}. \qquad (2)$$

In the limit of a circular orbit ($e \to 0$), the spin frequency matches the orbital frequency, with a ratio $P_{\mathrm{PSR}}/P_{\mathrm{orb}} \to 1$. As $e \to 1$, this ratio approaches zero. For modest eccentricities the ratio is of order unity; here we consider such cases of rotation rate as characteristic "slow" rotators.[7] For higher eccentricities the ratio decreases precipitously, but only reaches periods as short as an Earth day under the MFA for $e > 0.99$ (Figure 1, Table 1). Therefore, for all eccentricities modeled in this work, we use an Earth-like rotation period as characteristically "fast" rotation for comparison.

The sub-stellar longitude for a planet with zero obliquity is given by

$$\phi_\star(t) = \phi_\star(t_0) - \omega_{\mathrm{rot}}(t - t_0) + [\nu(t) - \nu(t_0)] \qquad (3)$$

---

[7] Venus is an example of a terrestrial-sized slow rotator in our own solar system, with a rotation period ≈116 Earth days and an orbital period of ≈224 Earth days, giving a spin–orbit rate ratio in the neighborhood of 2:1 (Bengtsson et al. 2013).
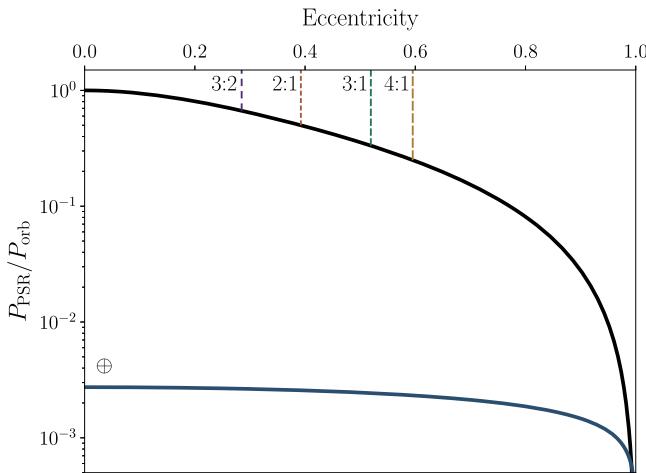
**Figure 1.** The theoretical pseudo-synchronous rotation period matches the synchronous period (orbital period) for a circular orbit, and remains of the order of the orbital period until very high eccentricity, where the ratio (shown in black) drops precipitously as $e \to 1$. Here we assume that the orbital period scales with the mean-flux approximation (Equation (1)), which preserves the orbit-integrated installation as eccentricity is changed. The ratio corresponding to a rotation period of one Earth day is shown as the curve in blue, labeled as $\oplus$. The values of eccentricity corresponding to spin–orbit resonances of 3:2 ($e = 0.285$), 2:1 ($e = 0.392$), 3:1 ($e = 0.519$), and 4:1 ($e = 0.595$) are marked.

where $\phi_\star$ is the sub-stellar longitude, initialized to $\phi_\star(t_0)$ at time t_0, $\omega_{\rm rot}$ is the angular rate of rotation, and ν is the true anomaly of the orbit. At high eccentricities, the sub-stellar point on the planet's surface exhibits a reversal of its direction of motion around periastron. This effect is due to the relation between the planet's rotation rate and the variable rate of change in true anomaly, and is also referred to as "optical libration." Works such as Selsis et al. (2013) and Bolmont et al. (2016) have demonstrated that, for models with planets on eccentric orbits and spin–orbit synchronization, the sub-stellar point will librate over an orbit, preventing perpetual day and night sides. Figure 2 shows this effect on the sub-stellar longitude as a function of eccentricity for PSR. The rate of change in anomaly $\dot\nu$ at periastron, relative to the mean motion $n \equiv 2\pi/P_{\rm orb}$, is

$$\frac{\dot\nu_{\rm peri}}{n} = \sqrt{\frac{1+e}{(1-e)^3}}. \qquad (4)$$

This evaluates to 5 for $e = 0.6$, compared with roughly 4 for $\omega_{\rm rot}/n$ under PSR. This transient increase in the rate of change in true anomaly causes it to exceed the rotation rate around periastron, during which time the sub-stellar point reverses direction from its otherwise westward motion.[8] While this effect can greatly expand the range of illuminated longitudes at high eccentricities for $\omega_{\rm rot}/n = 1$, for pseudo-synchronization the range of this motion is limited to a few degrees around the sub-stellar longitude around periastron, remaining close to an approximation of tidal locking. The resulting effect is that a significant fraction of the period of greatest installation is spent concentrated on a confined set of longitudes, rather than distributed nearly uniformly as in the fast-rotation case. This concentration of stellar heating drives strong thermal and

---

[8] This also happens, for example, on Mercury, whose moderate orbital eccentricity of ≈0.2 and spin–orbit rate ratio of 3:2 cause this effect.
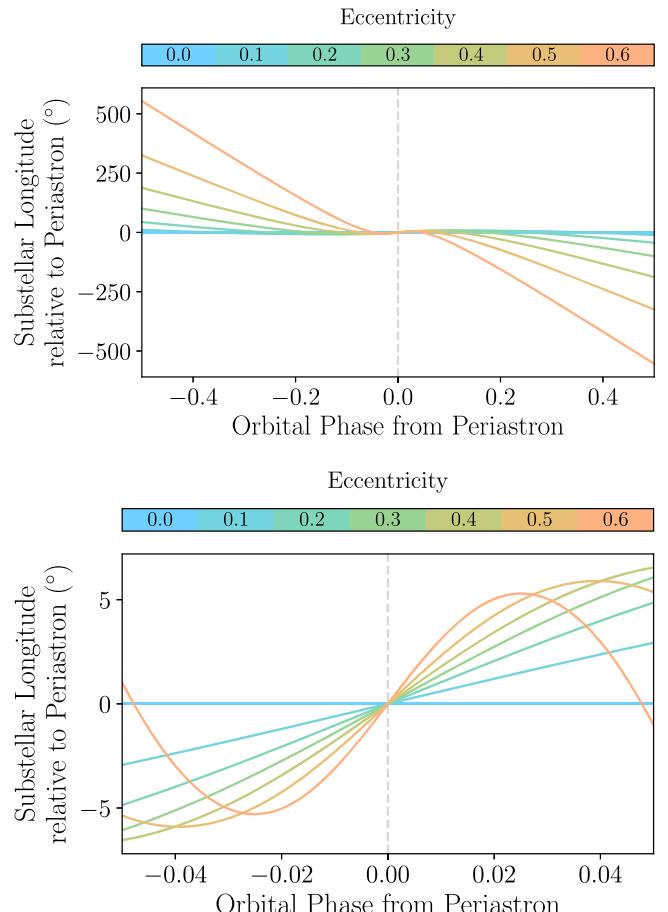

Figure 2. Eccentric orbits have periodically varying rates of change in the planet's orbital anomaly, with a maximum rate at periastron. For slow enough rotation (e.g., pseudo-synchronization), there exists a region of time around periastron where the instantaneous change in anomaly exceeds the rotation rate, causing the sub-stellar point on the planet's surface to move eastward rather than westward. This region is broad and the effect minor for nearly circular orbits, but narrow and increasingly intense at higher eccentricity. The plots show the movement of the sub-stellar longitude relative to its periastron position, both for one full orbit (top) and for a small region of orbital phase space around periastron (bottom), to show the effects at high eccentricity.

dynamical responses in the atmosphere, whose observable effects we detail in Section 4.

3. Model Details

The National Center for Atmospheric Research (NCAR) Community Atmospheric Model (CAM) is a global model designed to simulate Earth's atmosphere (Neale et al. 2010), and is the atmospheric component of the fully coupled Community Earth System Model (CESM). The physical evolution of the atmosphere in CAM is represented by the Navier–Stokes equations under the approximations of vertical hydrostatic equilibrium and a shallow aspect ratio of the flow, which together constitute the primitive equations. The primitive equations are implemented in a finite-volume dynamical core that uses horizontally Eulerian and vertically Lagrangian discretization to account for the grid-scale motions of dry air (Lin & Rood 1996, 1997), with additional conservation equations for water. The dynamical core conserves mass, momentum, and total energy with numerics that ensure physical tracers (e.g., water vapor) remain non-negative at each time step (Neale et al. 2010). A suite of sophisticated

algorithms are used to represent the net effect of subgrid-scale processes on the grid-scale variables; the subset of these parameterizations that seem most relevant to observables are described in the remainder of this section.

Here we use an adaptation of the ExoCAM[9] extension of CAM 4. Short for Exoplanet CAM, ExoCAM is designed for studies of both exoplanets and deep-time paleoclimates on Earth, with particular attention to expanding the valid ranges of stellar forcing, atmospheric partial pressures of greenhouse gases (H_2O, CO_2, and CH_4) (Wolf & Toon 2013, 2014), and planetary rotation rate. In particular, ExoCAM improves one of the numerical solvers in the deep convection scheme, using the more robust approach of Brent (1973, courtesy C. A. Shields). This scheme attempts to represent the effect of the total vertical mass flux in ensembles of cumulus clouds on grid-scale atmospheric temperatures and humidities. ExoCAM also includes improved substepping in the dynamical core, by applying fractional physics tendencies across the dynamical substeps instead of only at the beginning of the time step (Bardeen et al. 2017). This feature improves the numerical stability of the model for slow rotators and high incident solar fluxes. ExoCAM also extended to higher temperatures the absorption coefficients for the correlated-k radiative transfer scheme. These features allow ExoCAM to operate under warm and moist greenhouse conditions, with mean surface temperatures $\lesssim 365$ K and water vapor partial pressures $\lesssim 0.2$ bar.

Our version of the model is similar to the configuration described in Kopparapu et al. (2017). The horizontal resolution is $4° \times 5°$, with 40 vertical levels ranging from a global mean surface pressure around 1 bar to a minimum pressure of 10^{-3} bar. We employ a commonly used aquaplanet configuration for simplicity: we fix the planetary radius and surface gravity to Earth values, and have flat topography covered by a slab ocean of uniform depth (Bitz et al. 2012). Most of our simulations use an ocean depth of 50 m, but we also ran with ocean depths of 10 m at $e = 0.3$ to study how our results might change with ocean depth (see Section 5). Ocean heat transport is neglected, but the model accounts for sea ice formation via the CICE model from Hunke & Lipscomb (2008). The albedos of the water ocean in both the visible and near-IR are tuned to 0.06 for direct and 0.07 for diffuse reflection, matching the values established in Shields et al. (2013).

Bulk microphysical processes of condensation, precipitation, and evaporation follow the methods of Rasch & Kristjánsson (1998). Deep convection is treated using the method of Zhang & McFarlane (1995), which has been further updated to include convective momentum transport and dilute entraining plumes (Raymond & Blyth 1986, 1992). A separate convective treatment is employed for shallow adjustments following Hack (1994). In each grid cell, changing amounts of water vapor are self-consistently handled, with the total parcel mass determined from advection, convection, turbulent mixing, and large-scale stable condensation and evaporation tendencies. Virtual temperature corrections account for variations in density and the specific heat of moist air. Cloud fractions are calculated separately for marine stratus, convective clouds, and layered clouds. The radii of cloud liquid droplets are assumed to be 14 mm everywhere in the model. The effective radii of ice cloud particles follow a temperature-dependent

---

[9] https://github.com/storyofthewolf/ExoCAM

Table 1
Orbital Properties for Pseudo-synchronously Rotating Planets with Earth-like Mean Instellation

e	a (au)	P_{orb} (days)	P_{rot}		$F_\star$ (W m^{-2})	
			(days)	(P_{orb})	Min.	Max.
0.3	**1.024**	**378.35**	**242.98**	**0.642**	**768**	**2648**
0.4	1.045	389.88	190.65	0.489	636	3462
0.5	1.075	406.81	145.01	0.356	523	4711
0.6	**1.118**	**431.74**	**105.89**	**0.245**	**425**	**6800**
0.7	1.183	470.11	72.30	0.154	336	10791
0.8	1.291	535.70	43.45	0.081	252	20400
0.9	1.515	680.78	18.96	0.028	164	59281

Note. The bold entries correspond to the scenarios explicitly modeled in this work.

parameterization and can vary from a few tenths of a micron to a few tenths of a millimeter.

The radiative transfer code uses the correlated-k absorption coefficients derived from the HITRAN 2012 spectral database using the HELIOS-K open-source spectral sorting program (Kopparapu et al. 2017) and the standard two-stream approach from Toon et al. (1989). The spectral binning (Table 2) encompasses the solar spectrum, spanning 0.2–12.2 μm (bands 1–35 in our numbering scheme), as well as the planet's thermal emission in the range 2.5–1000 μm (bands 24–42). The spectral intervals used to calculate the relevant stellar and planetary fluxes are often referred to as the "shortwave" and "longwave," which are not strict divisions since the wavelength ranges overlap in ExoCAM. Accordingly, we use the ExoCAM solar spectrum for our stellar fluxes. Our initial atmosphere is assumed to be purely N_2, with the only greenhouse gas being H_2O drawn from the surface ocean; the water vapor continuum is treated using the formalism of Paynter & Ramaswamy (2011). The radiative effects of cloud overlap are treated using the Monte Carlo Independent Column Approximation, assuming maximum random overlap (Pincus et al. 2003).

3.1. Orbital Configuration

We ran models at orbital eccentricities of 0.3 and 0.6, modifying the orbital calculations used in the standard ExoCAM code to ensure greater accuracy at high eccentricity. For high eccentricities, calculating the orbital position is crucial for correctly modeling the sub-stellar position and time-dependent instellation. By default, CESM calculates the true longitude (corresponding to the true anomaly for exoplanets) of the Earth using an approximation given by a third-order polynomial,

$$\lambda = M + \left(2e - \frac{e^3}{4}\right)\sin(M + \varpi)$$
$$+ \frac{5e^2}{4}\sin[2(M + \varpi)]$$
$$+ \frac{13e^3}{12}\sin[3(M + \varpi)], \quad (5)$$

where M is the mean anomaly, e is the orbital eccentricity, and ϖ is the longitude of periastron. This approximation is valid to $\lesssim 0.3\%$ for eccentricities up to 0.1. However, the approximation rapidly diverges from the exact result, with the error reaching $\approx 12\%$ at $e = 0.5$, and $\approx 83\%$ at $e = 0.95$. We replace the

Table 2
Wavelength Ranges of Model Spectral Bands

Band	λ_{start}	λ_{mid} (μm)	λ_{end}	Brightness Temp. (K)
1	0.200	0.227	0.263	11011–14489
2	0.263	0.299	0.345	8404–11011
3	0.345	0.387	0.442	6563–8404
4	0.442	0.477	0.518	5593–6563
5	0.518	0.567	0.625	4636–5593
6	0.625	0.642	0.660	4390–4636
7	0.660	0.676	0.692	4187–4390
8	0.692	0.717	0.743	3898–4187
9	0.743	0.760	0.778	3724–3898
10	0.778	0.811	0.847	3419–3724
11	0.847	0.877	0.909	3188–3419
12	0.909	0.952	1.00	2898–3188
13	1.00	1.05	1.10	2637–2898
14	1.10	1.17	1.24	2333–2637
15	1.24	1.27	1.30	2231–2333
16	1.30	1.36	1.43	2028–2231
17	1.43	1.47	1.50	1927–2028
18	1.50	1.56	1.63	1782–1927
19	1.63	1.69	1.77	1637–1782
20	1.77	1.85	1.94	1492–1637
21	1.94	1.99	2.04	1420–1492
22	2.04	2.09	2.15	1347–1420
23	2.15	2.31	2.50	1159–1347
24	2.50	2.76	3.08	942–1159
25	3.08	3.42	3.84	753–942
26	3.84	4.02	4.20	690–753
27	4.20	4.37	4.55	638–690
28	4.55	4.67	4.81	603–638
29	4.81	5.15	5.56	522–603
30	5.56	6.10	6.76	429–522
31	6.76	6.97	7.19	403–429
32	7.19	7.78	8.47	342–403
33	8.47	8.77	9.09	319–342
34	9.09	9.62	10.20	284–319
35	10.20	11.11	12.20	238–284
36	12.20	13.16	14.29	203–238
37	14.29	15.04	15.87	183–203
38	15.87	17.70	20.00	145–183
39	20.00	21.62	23.53	123–145
40	23.53	25.81	28.57	101–123
41	28.57	36.36	50.00	58–101
42	50.00	525	1000	3–58

Note. Bands 30–41 were used in our analysis. We include the entire model spectral output for completeness.

approximation with a simple numerical method that iteratively solves Kepler's equation,

$$M = E - e \sin E, \tag{6}$$

where E is the eccentric anomaly.

3.2. Observable Properties

We now describe how we simulate the radiation that would be observed by a telescope at a location distant from the planet and star of interest. Exoplanetary systems can in general have any possible orientation with respect to the observer. For our full-phase analyses we restrict ourselves to two lines of sight, both edge-on with respect to the orbital plane: one along the periastron–star line and the other along the apastron–star line (Figure 3). This amounts to varying the longitude of periastron
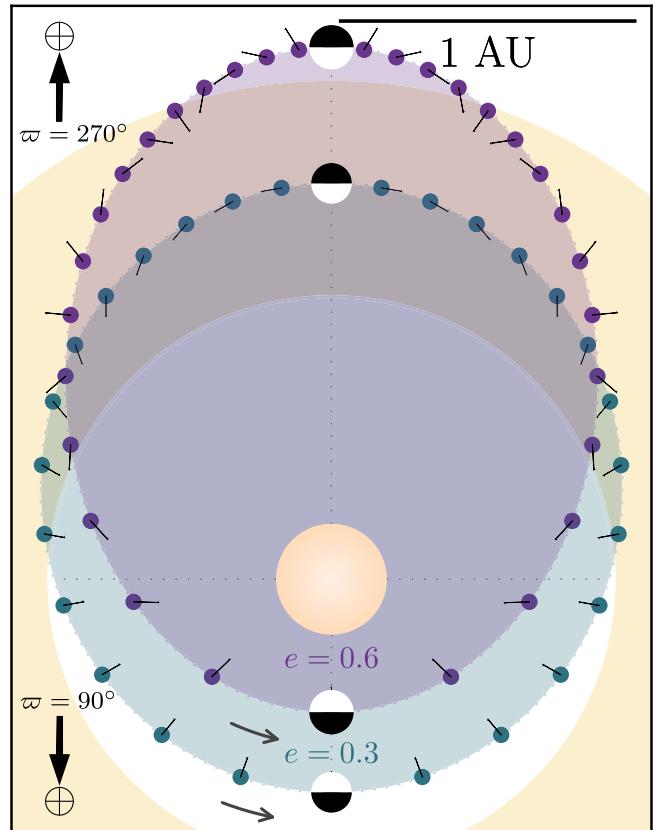

Figure 3. We consider two orbital eccentricities (0.3 and 0.6), each from two possible edge-on viewing geometries. At $\varpi = 90°$, we see the planet's night side (anti-stellar hemisphere) during its periastron passage, and the day side (sub-stellar hemisphere) during apastron. At $\varpi = 270°$, the day-side viewing is aligned with periastron, and the night-side during apastron. The limits of the Habitable Zone from Kopparapu et al. (2014) are plotted as a golden annulus for Earth-mass planets, with the "Runaway Greenhouse" and "Maximum Greenhouse" limits setting the inner and outer radii, respectively. The colored dots represent points equally spaced in time, at intervals of $\approx$13.5 days; their poles show the rotation through one orbit (from apastron to apastron) for pseudo-synchronous rotation.

while keeping other orientation parameters fixed. In the first case (corresponding to an inclination $i = 90°$, longitude of periastron $\varpi = 90°$), one would observe the night side of the planet during periastron, when the planet would transit its host star; then, one would be able to see the day side during apastron, when the planet passes through its secondary eclipse. In the second case ($i = 90°$, $\varpi = 270°$), the day side is visible during periastron (or more precisely, just before and after eclipse), and the night side (transit) at apastron. In addition to these two cases, we also generate theoretical eclipse depths for the full possible range of longitudes of periastron, in order to show the variation in day-side emission with viewing geometry.

To generate theoretical light curves, we take the outgoing radiation maps in each model band and calculate the expected observable flux for a given viewing geometry. We use the ExoCAM solar spectrum for the model host star to then express our expected brightnesses in units of the thermal stellar flux. To compare with a realistic set of observations in the infrared, we adopt the wide filter profiles for the Mid-Infrared Imager (MIRI, see Space Telescope Science Institute 2018) on the *James Webb Space Telescope* (*JWST*, see Glasse et al. 2015; Rieke et al. 2015; Wright et al. 2015). These filters span a range
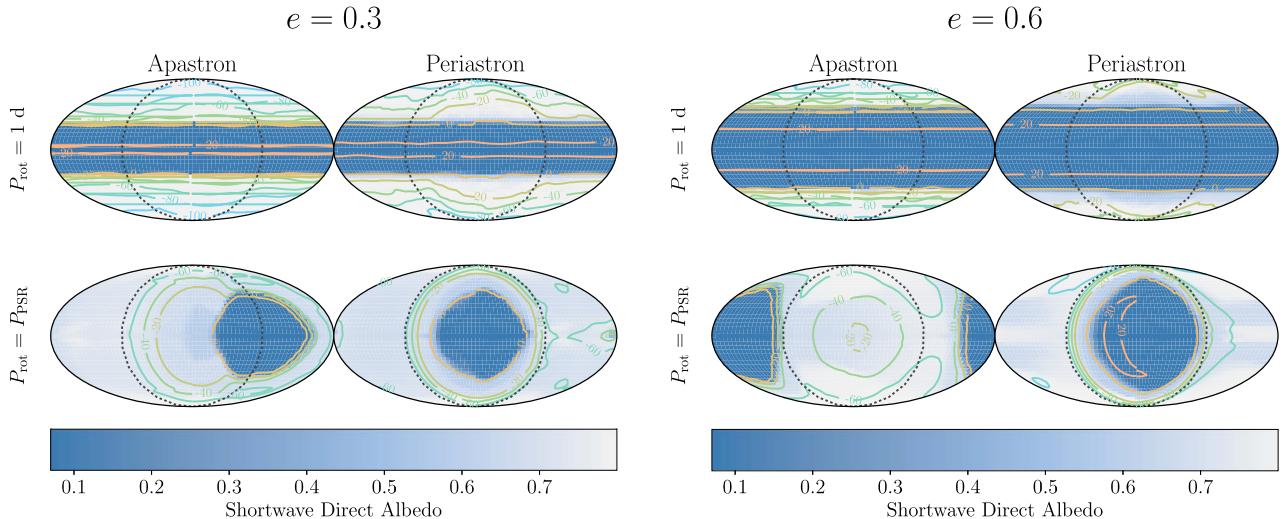
Figure 4. Global maps of the diffuse shortwave albedo at the surface at the extreme points of each orbit, shown for fast rotation (Earth-like, in the upper row) and the much slower pseudo-synchronous rotation (defined in Equation (2), in the lower row), at orbital eccentricities of 0.3 and 0.6. The dark dotted lines delineate the star-facing hemisphere, which is centered in each plot. Colored contours denote surface temperature in degrees Celsius. The nominal albedo for liquid water is taken to be 0.06–0.07 (see Section 3 for details), and the limiting albedo for thick ice cover is 0.8.

of approximately 5–30 μm. Convolving these filter profiles with the model bands, we generate emission maps for each MIRI filter.[10] Given an emission map $M_\lambda(\phi, \theta, t)$ at a specific wavelength, we solve for the corresponding planet–star flux contrast via

$$\bar{F}(t) = \frac{1}{\pi}\left(\frac{R_p}{R_\star}\right)^2 \frac{\iiint w M_\lambda V \, d\lambda \, d\theta \, d\phi}{\int w F_{\lambda,\star} \, d\lambda} \qquad (7)$$

where $w = w(\lambda)$ is the weighted response of the instrumental bandpass at λ, $V = V(\phi, \theta, t)$ is the component of the normal vectors of the planet grid cells along the line of sight, and $F_{\lambda,\star}$ is the disk-integrated stellar flux at λ. For a sub-observer point given by longitude $\phi_{\rm obs} = \phi_\star(t_{\rm ecl}) - \omega_{\rm rot}(t - t_{\rm ecl})$ for rotation rate $\omega_{\rm rot}$ and the midpoint time of the reference eclipse satisfying $\nu(t_{\rm ecl}) = \frac{3}{2}\pi - \varpi$, and latitude $\theta_{\rm obs} = 0$,

$$V = \begin{cases} \cos(\phi - \phi_{\rm obs})\cos\theta, & \cos(\phi - \phi_{\rm obs}) \leqslant \pi/2 \\ 0, & \cos(\phi - \phi_{\rm obs}) > \pi/2. \end{cases} \qquad (8)$$

Once we have a full orbit of predicted photometry, we select the contrasts during eclipse as our predicted eclipse depths.

Each model is run for 25 orbital periods; this value was chosen as the longest time needed (across all of our integrations) for the range of global mean, time mean surface temperatures for each of a span of 10 orbits to be within 1% of the global mean, time mean temperature averaged over the same 10 yr span. Within the final 10 yr, the model also remains within 0.25 W m^{-2} of global, annual mean radiative balance at the top of the atmosphere. Our spin-up time of 15 yr is similar to other slab-ocean GCM simulations, matching for example that of Chiang & Bitz (2005), who also use ocean mixed layer depths of 50 m. The model photometry we present accordingly uses statistics calculated for the final 10 orbits of each simulation.

---

[10] These bands are adopted as a template for mid-infrared photometry. The precision required to discern the variations in this study will be outside the scope of *JWST* itself; for a discussion of the potential for future observations, see Section 5.

Table 3
Global Ranges and Means of Surface Temperature (K)

		Earth-like			PSR		
e	Time	Range	Mean	Ocean Mean[a]	Range	Mean	Ocean Mean[a]
0.3	Apo	155–295	220	288	198–286	228	280
	Peri	170–295	241	289	195–285	228	278
0.6	Apo	183–305	248	292	200–287	228	280
	Peri	214–305	271	293	191–298	232	285

Note.
[a] The ocean mean is defined as the global mean of all regions with $T > 273.15$ K.

4. Results
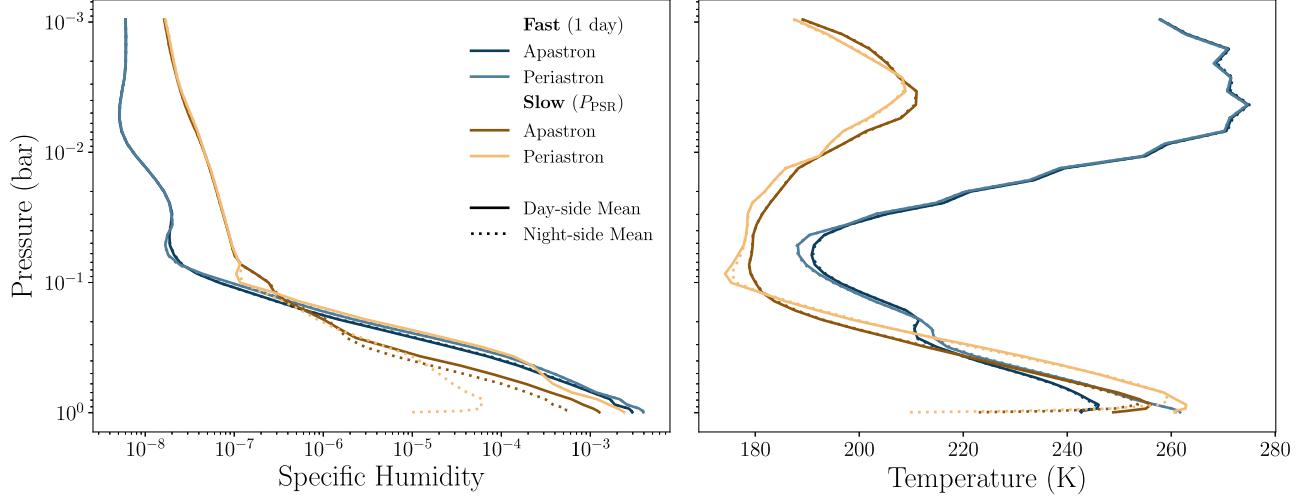
4.1. Internal Results

In this section we describe the simulated climate of our four hypothetical planets, then illustrate a key difficulty in interpreting observations of such planets: temperatures in the upper troposphere near the emission level vary because of both day–night contrast and orbital periodicity, with the amplitude and phase of these variations being highly sensitive to orbital eccentricity.

4.1.1. Surface Conditions

Rotation rate strongly influences horizontal temperature gradients, as expected, with fast rotation confining warm air near the equator and producing strong eastward winds that homogenize energy content in longitude. This is clearly seen in the distributions of surface temperature and surface albedo, with the latter indicating the regions covered by sea ice on these aquaplanets (Figure 4 and Table 3). Contrasts in temperature and albedo are primarily latitudinal for Earth-like rotation, and are accompanied by a Hadley circulation with a rising branch centered on the equator. For slow PSR, longitudinal contrasts are just as strong as latitudinal ones, with warm, ice-free oceans centered on the sub-stellar points at periastron and ice-covered regions extending over the night
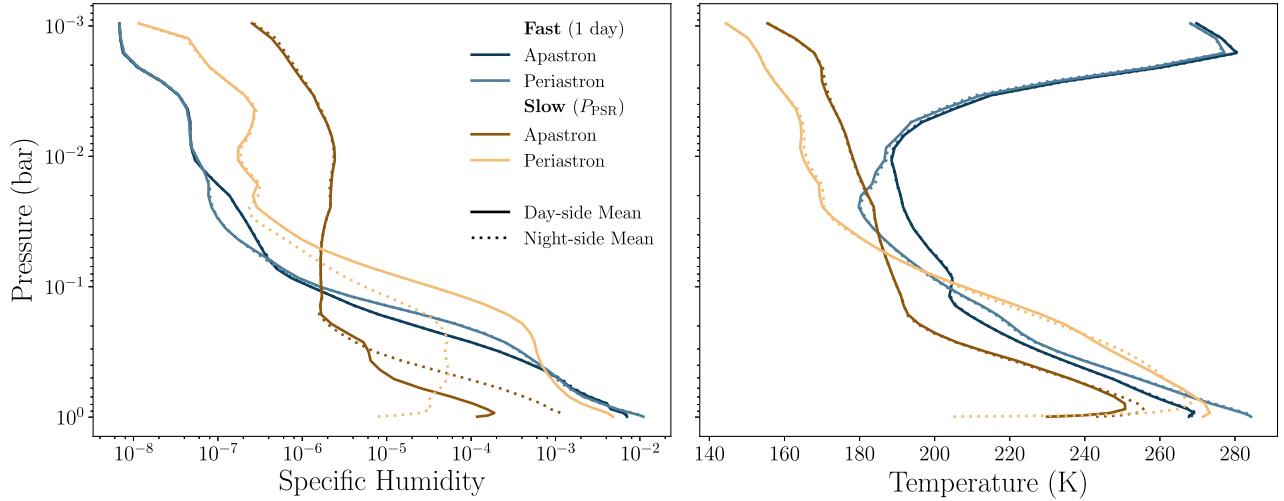
Figure 5. The specific humidity (fraction of atmospheric mass in H_2O) and temperature, both averaged over the day sides (solid lines) and night sides (dotted lines). Each color represents a rotation period: the bluer hues show fast (Earth-like) rotation, and the golden hues show slow (pseudo-synchronous) rotation. The lighter shades represent each quantity during periastron, and the darker shades each during apastron.

side and polar regions. The slow-rotator circulation patterns are also much broader in latitude than their fast counterparts, in agreement with the circulation patterns seen in previous simulations of aquaplanets at different rotation rates, e.g., Figure 6 in Merlis & Schneider (2010). At apastron, the effects of ocean thermal inertia and deviations from strict synchronous rotation combine to shift the warm, ice-free region away from the sub-stellar point. For $e = 0.3$ and slow rotation, the ice-free region straddles the day–night line at apastron; for $e = 0.6$ and slow rotation, the ice-free region is actually on the night side of the planet at apastron while the day side is ice-covered and has a secondary temperature maximum of about $-20°C$ at the sub-stellar point.

The horizontal range in surface temperature at both extremes of the orbit is larger for fast rotation than for slow, implying that rotational confinement by the atmospheric circulation is more effective at generating horizontal temperature gradients than the day–night contrast in radiative heating. In fact, both the range and global mean of surface temperatures for the $e = 0.3$, slow-rotation case are remarkably similar between

apastron and periastron. Cowan et al. (2012) calculated that, for a terrestrial planet, the effective thermal relaxation times for snowball and temperate (ocean) climates are ~145 and 343 days, respectively. Given that this scale is much longer than the analogous timescales expected for much of the atmospheres of eccentric Hot Jupiters (e.g., Kataria et al. 2013; de Wit et al. 2016), it is not surprising that contrasts in surface temperature between the extremes of the orbit are quite muted for the slow rotator. The differences in apastron-to-periastron global mean temperature for the fast rotators at both eccentricities exceed $20°C$, a greater but still modest contrast given the differences in instellation between the extremes of the orbits.

4.1.2. Atmospheric Conditions

Temperature contrasts are even more muted between the day and night sides of the slow rotator in the atmosphere above the lowermost troposphere (Figure 5, right column). This is expected because the Rossby deformation radius is larger than the planetary circumference at these rotation rates, allowing

atmospheric circulations to rapidly homogenize temperatures throughout most of the troposphere, as in previous studies of strict synchronous rotation (e.g., Joshi et al. 1997). But in contrast with those previous studies, the shallow, near-surface temperature inversion that forms on the ice-covered side of the planet is actually on the day side of the planet at apastron (see the bottom right panel of Figure 5), due to the combined effects of ocean thermal inertia and deviations from strict synchronous rotation, as discussed above. As noted in Section 4.1.1, the thermal timescales for surface ice and water are much longer than the timescales at equivalent temperatures in the upper atmosphere, which themselves are longer than the typical Hot Jupiter timescales due to the much lower average atmospheric temperatures for the ocean planets (Showman & Guillot 2002; Showman et al. 2010).

To illustrate how these effects might complicate interpretation of observations, we plot time series, over an orbit, of the day- and night-side temperatures averaged over an atmospheric layer near the emission level, which we estimate to be ~0.3 bar (Figure 6). In an optically thick atmosphere, radiative emission might come from this upper-tropospheric layer, making its temperature more relevant to observations than surface conditions. The behavior of the fast rotator is easy to understand, with day- and night-side temperatures being nearly equal, and peak temperatures reached shortly after periastron for both eccentricities. For the slow rotator, the day–night contrast in upper-level temperature is also very small, and the orbital variations in emission from this level are due almost entirely to changes in planet–star distance. It would thus be difficult to distinguish a fast rotator from a slow rotator given only emission from this upper-tropospheric level. In contrast, surface temperature exhibits a large contrast between day side and night side on the slow rotators. Night-side surface temperature has the same range as the temperature at 0.3 bar but with the opposite phase for $e = 0.3$; for $e = 0.6$, night-side surface temperatures for the slow rotator show several peaks over an orbit, corresponding to the roughly four rotations that occur over an orbit at this eccentricity (Figure 1). Thus, inferences about rotation rate would be most easily made from the day–night contrast in surface temperature, but it is possible that emission will come from a much higher altitude.

The troposphere of the slow (pseudo-synchronous) rotator exhibits a much wider longitudinal contrast in water content than in temperature (Figure 5, left column). As we move from the surface to the upper troposphere, the slow rotator retains a much moister troposphere on the day side at periastron, even though temperatures are nearly equal above the lower-tropospheric inversion layer. This is also true at apastron for $e = 0.3$, but for $e = 0.6$ at apastron the humidity is higher over the open ocean on the night side and lower over the ice-covered surface on the day side. Considering the slowly rotating case further, we notice that the strong wet–dry difference extends to ~0.1 bar at periastron for $e = 0.3$, compared with a weaker wet–dry difference extending to ~0.25 bar at apastron. This reflects the large warming and deepening of the troposphere over the sub-stellar point when the radiative forcing is strongest at periastron. The day–night humidity contrast seen on the slow rotator is even more pronounced at higher eccentricity, reaching ~0.03 bar. The upper troposphere at apastron is warmer and more humid at the sub-stellar point than at the anti-stellar point, even though the converse is true at
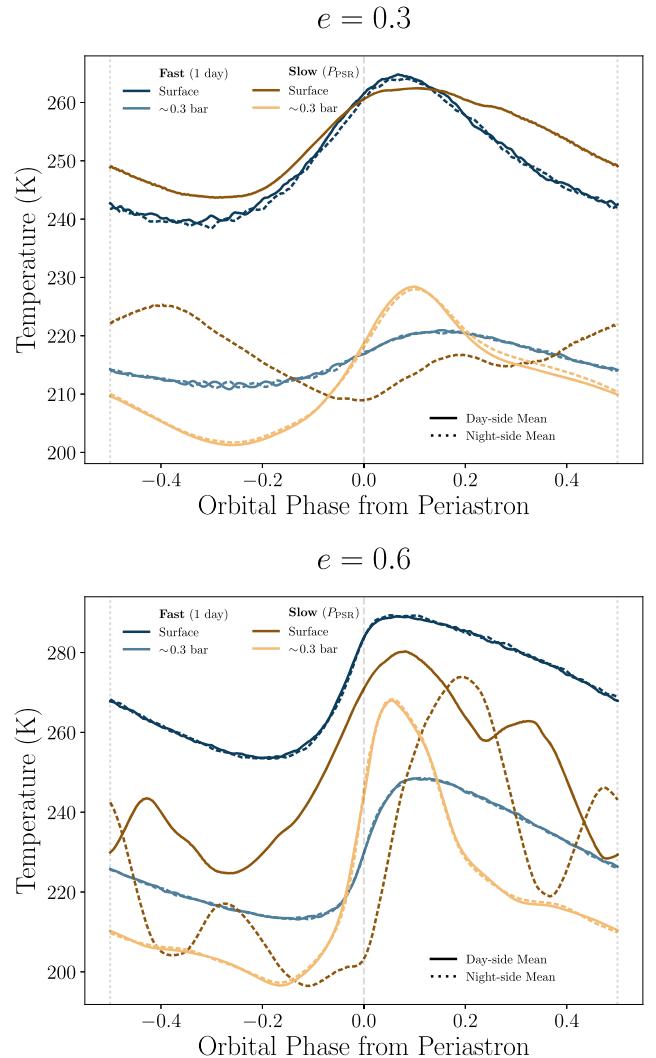

Figure 6. Time series of hemispherically averaged temperatures over one orbit. Each color represents a rotation period: the bluer hues show fast (Earth-like) rotation, and the golden hues show slow (pseudo-synchronous) rotation. Lighter shades are the temperatures at the effective emission layer (taken to be centered at ~0.3 bar, averaged over 0.2–0.4 bar), and darker shades are surface temperatures. The solid lines are the averages over the day sides and the dotted lines the averages over the night sides. At the surface, day–night contrasts in temperature are comparable in amplitude to the variations due to the orbital periodicities in insolation. However, in the upper troposphere, from where outgoing emission may originate in many longwave spectral bands, the day–night contrasts are effectively negligible.

the surface and in the lower troposphere, showing the complexity introduced to day–night contrasts by PSR.

Given these strong day–night contrasts in humidity, it is not surprising that the slow rotators at both eccentricities show extremely large cloud water paths (vertically integrated condensed water in cloud droplets), approaching $1 \, \mathrm{kg \, m^{-2}}$ following periastron,[11] centered on the sub-stellar point at periastron (Figure 7), and largely mimicking the features seen in both surface temperature and albedo. The negative cloud forcing in the shortwave is presumably responsible for limiting sub-stellar surface temperatures at periastron, causing the peak ocean temperatures to exist in a partial ring around the sub-stellar point (Figure 4).

---

[11] For comparison, the same mass surface density in Earth's tropics peaks near $200 \, \mathrm{g \, m^{-2}}$ (O'Dell et al. 2008).
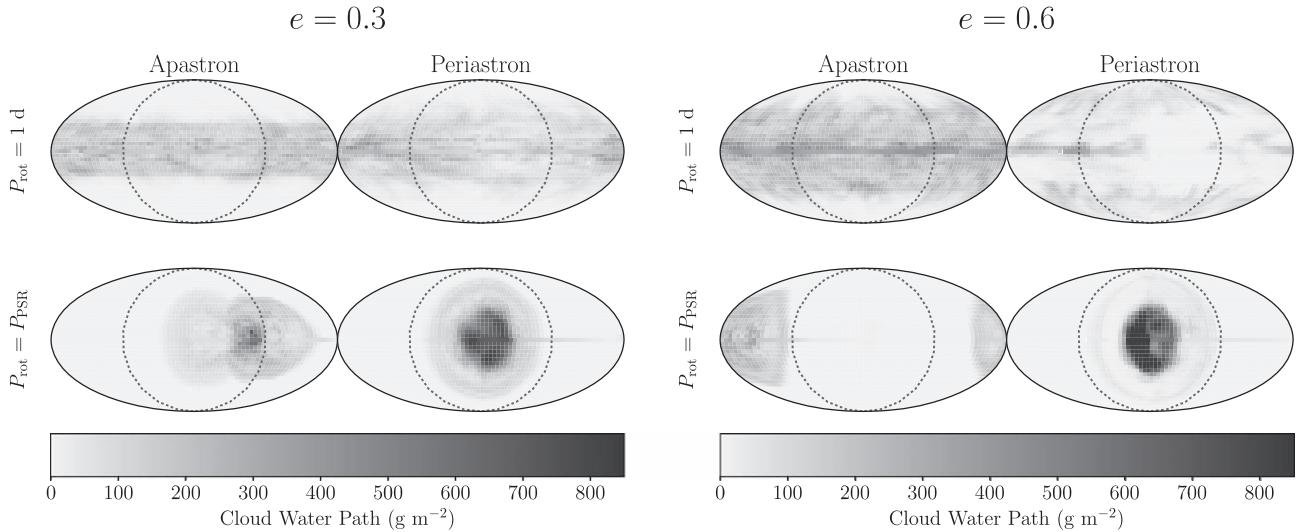
Figure 7. Global maps of the vertically integrated condensed cloud water at the extreme points of each orbit, shown for fast rotation (Earth-like, in the upper row) and the much slower pseudo-synchronous rotation, defined in Equation (2), in the lower row, at orbital eccentricities of 0.3 and 0.6. The dark dotted lines delineate the star-facing hemisphere, which is centered in each plot.

Taken together, all of these quantities show that slowly rotating planets on orbits of modest to high eccentricity can become mostly ice-covered, except for a longitudinally confined warm, cloudy, and ice-free region region that persists at low latitudes through the orbit. This is consistent with previous simulations of synchronously rotating aquaplanets on circular orbits (e.g., Joshi et al. 1997; Merlis & Schneider 2010) and on eccentric orbits (Bolmont et al. 2016), except that the ice-free region does not remain on the day side at apastron for PSR (see Section 4.2.2 for further discussion). The implications of this shift in the warm, ice-free region for observable emission are further complicated by the fact that atmospheric temperatures vary much more than surface temperatures over the orbit (e.g., Figure 5), responding to the orbital cycle of instellation. In contrast, for faster, Earth-like rotation, all quantities are homogenized longitudinally, so that outgoing radiation will be set by the orbital variations in stellar heating.

4.2. External Results

4.2.1. Outgoing Longwave Radiation

As an intermediate step between characterizing the atmospheric state and simulating what might be observed by a telescope, we examine the horizontal distribution of planetary radiative emission in the spectral bins used by the model radiation scheme. The peak radiative flux in each spectral bin is similar (within $\pm 50\%$) across rotation rates and orbital phase. The fast rotators have emission that is nearly uniform in longitude with large equator-to-pole gradients, as expected. In contrast, the night-side fluxes of the slow rotators at most wavelengths remain much lower when compared to either the slow-rotation day-side fluxes or the fluxes in the equatorial regions of the fast rotators (Figure 8). In all bands, the slow-rotation sub-stellar point is an emission minimum due to the thick cloud shield, and the maximum emission occurs in a ring closer to the edge of the day side.

The contrast between night-side emission and the emission from this ring at the edges of the day side is weaker in the 6.97 and 7.78 μm bands, which both lie in the absorption band for water vapor that is centered at 6.3 μm (and which, in turn,

absorbs strongly between 5 and 8 μm). In these spectral regions, the dryness of the atmosphere on the cold night side allows radiation to escape from the lower troposphere or the surface itself, while the high optical depth on the warm day side allows emission only from higher (and thus colder) levels of the upper troposphere. The day–night contrast for slow rotation also weakens for the same reasons as we move out beyond 20 μm into the reddest bands occupied by the rotational absorption features of water.

These emission distributions show that the strong longitudinal temperature contrasts in our slow rotators are best observed in longwave bands away from the major water vapor absorption features. When considering observables, it must also be borne in mind that for a non-tidally locked planet, the warm side will not always be the day side (e.g., Figure 4). Changes in emission caused by variations in planet–star distance over an orbit may also complicate the inferences that can be made about rotation rate from observables. This motivates construction of simulated light curves in the next section.
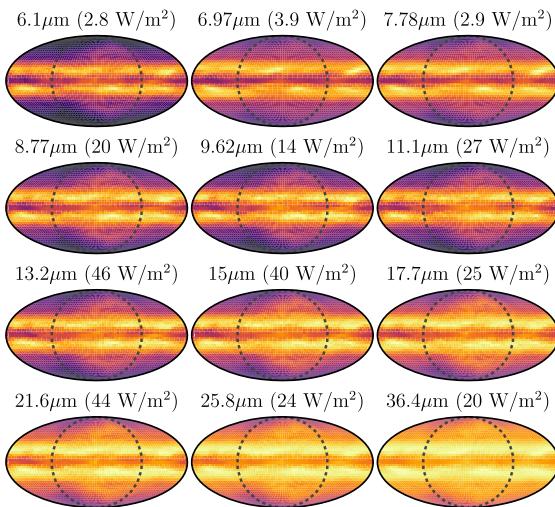
4.2.2. Observable Light Curves

Adopting the methodology of converting model output to photometry, we generate light curves based on the *JWST* MIRI filter profiles, for the two assumed viewing geometries described in Section 3.2. Figure 9 shows the model light curves at both eccentricities for a viewing geometry where the planet's transit and periastron passage coincide ($\varpi = 90°$), and Figure 10 shows light curves for a geometry where eclipse and periastron passage coincide ($\varpi = 270°$). We discuss four primary qualities of these light curves.
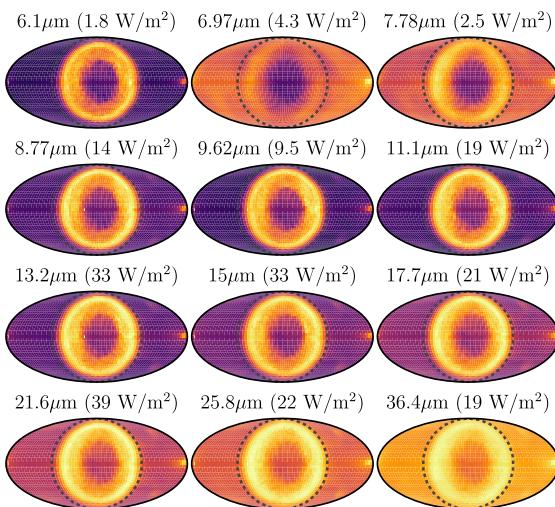
1. For Earth-like rotation, the variation follows the expectation for a longitudinally symmetric system in which the flux follows the variations in planet–star distance over the orbital cycle, modified by the viewing geometry. Accordingly, the variations in the light curve have significantly higher amplitude at higher eccentricity (note the change in vertical scale between eccentricities in Figures 9 and 10). The light curves for fast rotators reach their peak at or shortly after apastron, when the planet is
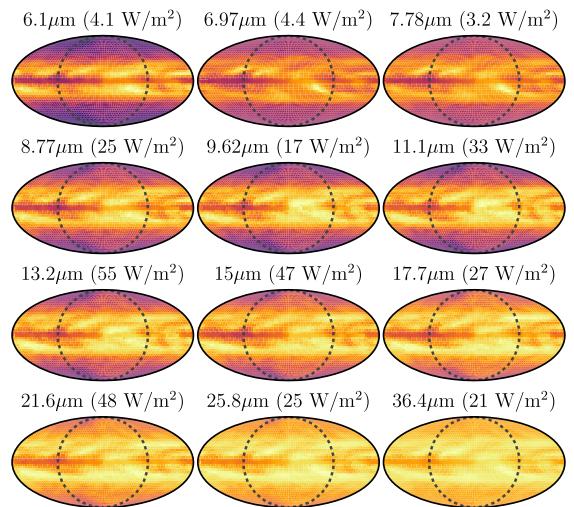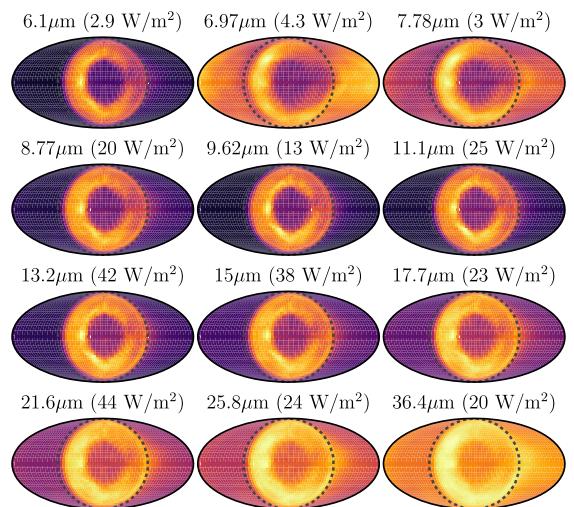
Figure 8. Global outgoing flux at the top of the atmosphere for a range of infrared bands from the ExoCAM model (bands 7–18 in Table 2), for each of the two rotation periods and orbital eccentricities, during periastron. The dotted lines delineate the star-facing hemisphere, which is centered in each plot. Each subplot has a color range with zero flux as black, and the brightest color given by the flux above each globe in parentheses.

closest to the star and thus hottest, and the light-curve morphology is largely independent of wavelength.

2. For PSR, the phase variations are more complicated but are generally affected strongly by the longitudinal temperature contrasts. Where eclipse aligns with periastron and thus the observer sees the day side (corresponding to $\varpi = 270°$, in Figure 10), the light curves have maxima at or just after periastron, giving the slow-rotation light curves similar times of extrema to the fast rotators for both eccentricities. Conversely, where eclipse is aligned with apastron ($\varpi = 90°$, Figure 9) the light curves reach an absolute minimum near periastron. For $e = 0.3$ the slow-rotation light curves are nearly 180° out of phase with the light curves for Earth-like rotation. In contrast, for $e = 0.6$ the

flux quickly brightens after the periastron minimum as the rotation in this part of the orbit brings the highly irradiated hemisphere into view, resulting in the maxima of the slow-rotation light curves occurring at nearly the same orbital phase as the maxima of light curves for fast rotation.

3. The fluxes of the slow rotator are consistently lower than their fast counterparts for $\varpi = 270°$ and for the high-eccentricity curves with $\varpi = 90°$. This is consistent with the slow-rotation cases having ice-covered sides substantially colder than the mean temperature of the fast rotators (Figure 4 and Table 3), as well as much higher upper-tropospheric humidities (Figure 5) on the warm sides of the planets, and therefore much larger cloud water paths (Figure 7).
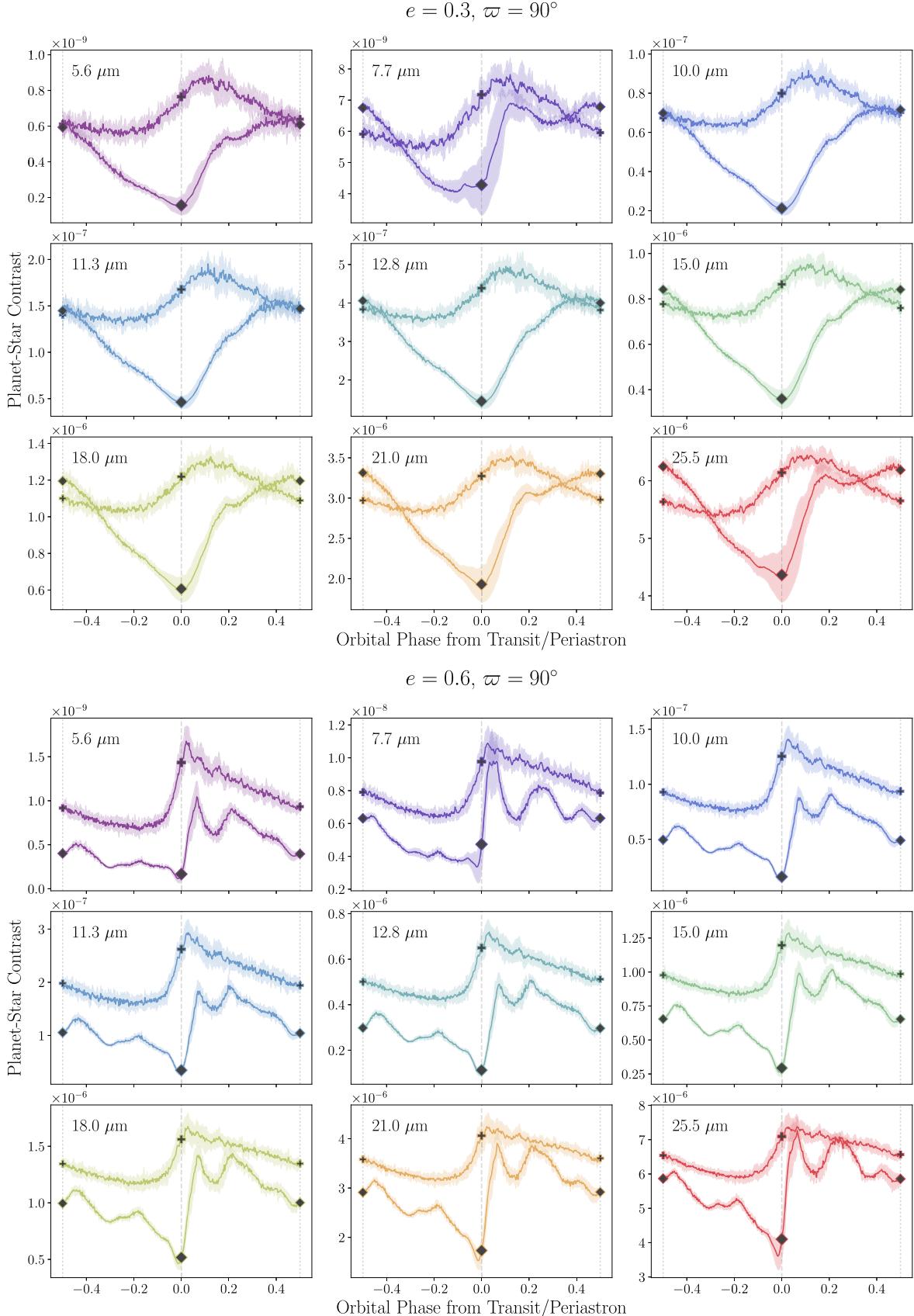
Figure 9. Simulated light curves for a viewing geometry such that the orbit is seen edge-on, and the planet transits during periastron. Each 3 × 3 grid represents one of the two orbital eccentricities. The light curves are plotted for each of the nine MIRI bands of the upcoming *James Webb Space Telescope*. Within each plot, the light curve with plus-sign markers shows Earth-like (fast) rotation, and the curve with diamond markers shows pseudo-synchronous (slow) rotation. The solid color lines are the averages over the final 10 orbits, and the surrounding shaded region represents the range of fluxes over the orbits.
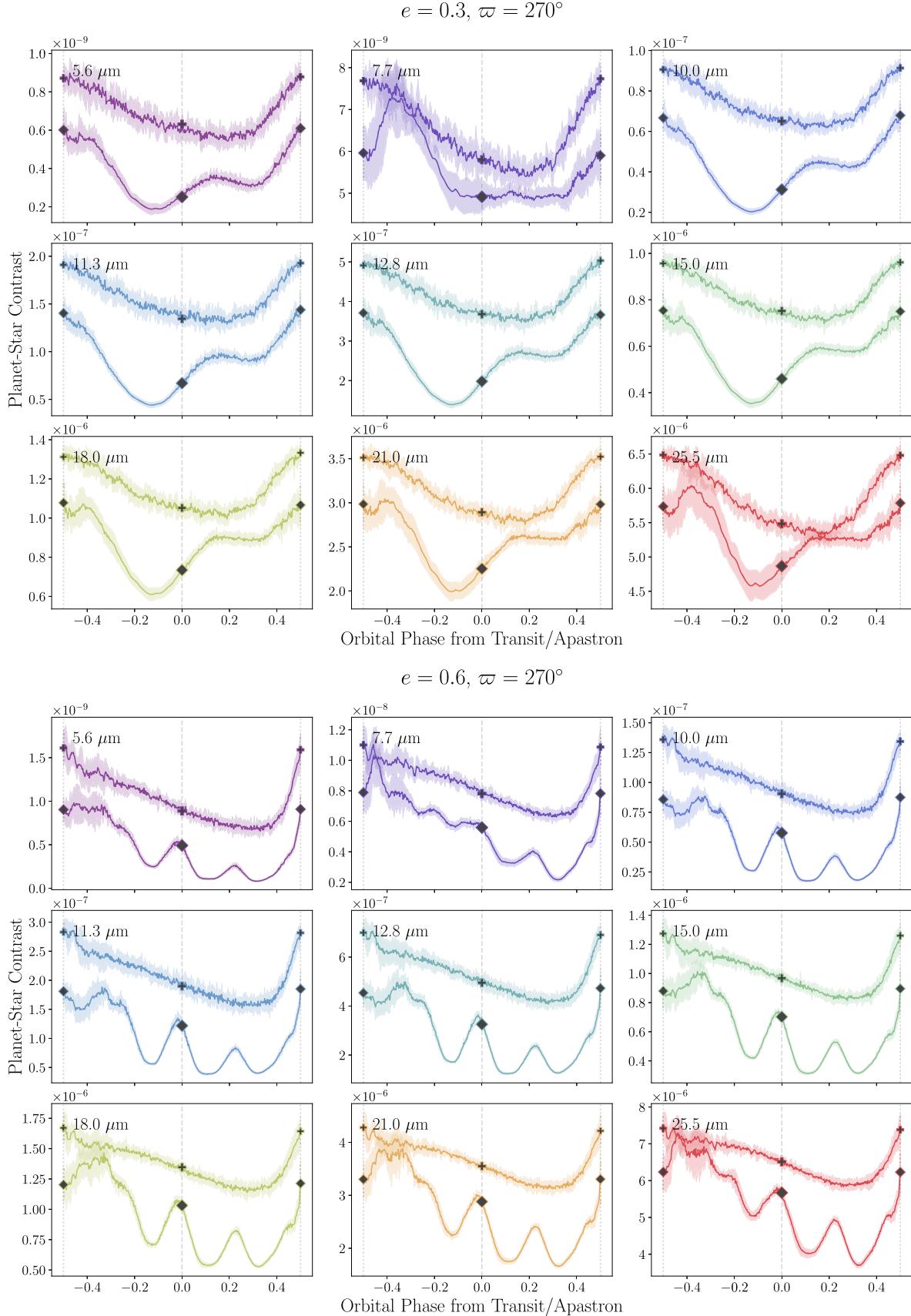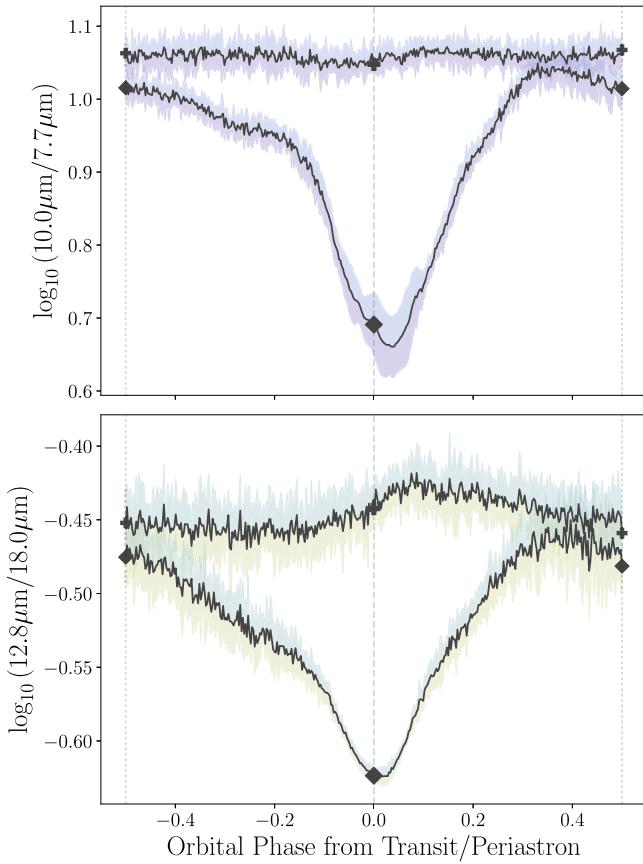
Figure 10. Simulated light curves for a viewing geometry such that the orbit is seen edge-on, and the planet undergoes secondary eclipse during periastron. Each 3 × 3 grid represents one of the two orbital eccentricities. The light curves are plotted for each of the nine MIRI bands of the upcoming *James Webb Space Telescope*. Within each plot, the light curve with plus-sign markers shows Earth-like (fast) rotation, and the curve with diamond markers shows pseudo-synchronous (slow) rotation. The solid black lines are the averages over the final 10 orbits, and the surrounding shaded region represents the range of fluxes over the orbits.
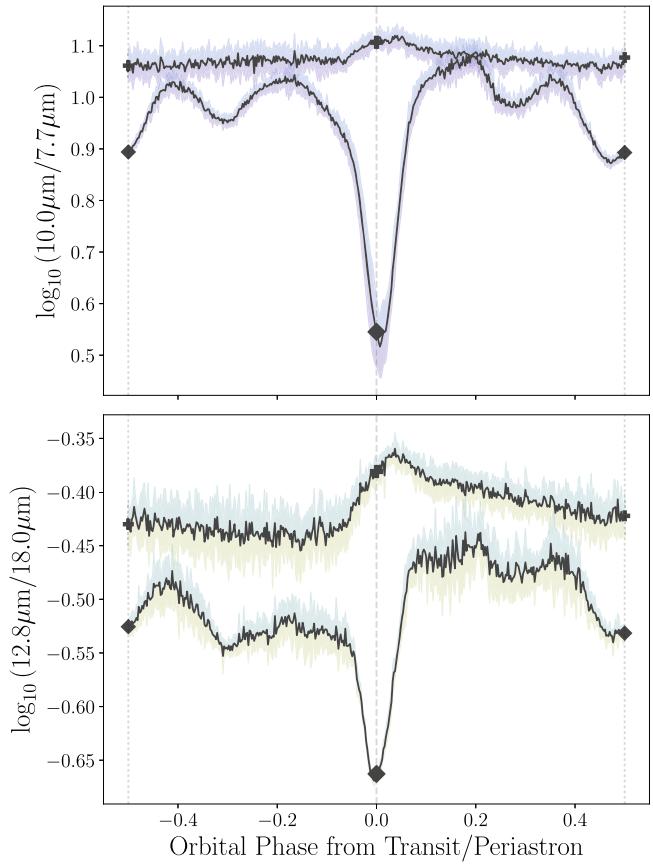
Figure 11. Ratios of a selection of the planet–star contrasts shown in the light curves of Figure 9, where the planet transits during periastron. Within each plot, the light curve with plus-sign markers shows Earth-like (fast) rotation, and the curve with diamond markers shows pseudo-synchronous (slow) rotation. The solid black lines are the averages over the final 10 orbits, and the surrounding shaded region represents the range of fluxes over the orbits. The choice of colors for these regions is purely to illustrate the fluxes used for each ratio.

4. The simple thermal expectation is that, as the bands move toward longer wavelengths, the contrast ratio will increase. We see this in both rotation rates, but additional wavelength-dependent features are present for slow rotation in particular that affect the shapes of the periastron-induced maxima for $\varpi = 270°$. For example, in the $e = 0.3$ light curves for the slow rotator, there are peaks shortly after periastron consistent with H_2O emission in the F770W band (centered at 7.7 μm) and at wavelengths longer than 18 μm. The increase in upper-atmosphere moisture content by an order of magnitude (as seen in Figure 5) provides the slower rotators with the water vapor needed to intensify the observed flux in this band.

Beyond these major features, some additional qualities of the light curves warrant explanation. Secondary peaks occur in most of the slow-rotation light curves and come from the ratio of the rotation period to the orbital period. This creates a single secondary peak for $e = 0.3$, where the ratio is ≈ 0.64 (i.e., roughly two rotations each orbital period), and three secondary peaks for $e = 0.6$, where the rotation period is close to one-quarter of the orbital period. This effect is often referred to as "ringing," and is due to the day-side hemisphere from periastron passage retaining a high temperature as it rotates in and out of view. Such an effect was predicted in the
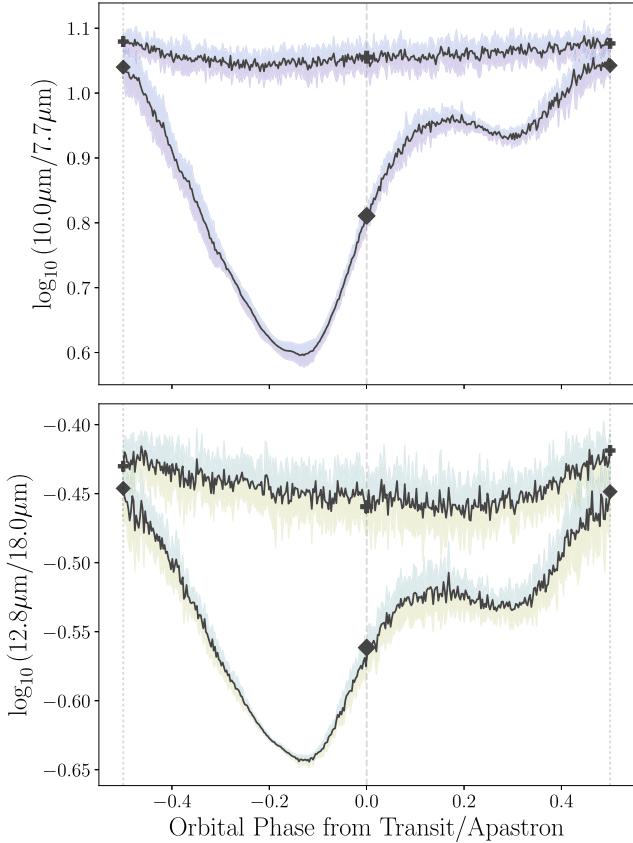
hydrodynamical simulations of Langton & Laughlin (2008) for planets such as HD 80606 b, and further seen in the models of Cowan & Agol (2011) and Kataria et al. (2013). The ringing only comes about for strong enough day–night temperature differences, and if both the thermal timescale and rotation period are shorter (though not significantly shorter) than the orbital period; this condition was used to constrain the rotation period of the highly eccentric HD 80606 b, whose phase variations have been observed not to exhibit this ringing behavior (de Wit et al. 2016; Lewis et al. 2017).

Finally, we note that the inter-orbital variability in flux is generally broader and more consistent over orbital phase for the fast rotators. For the slow rotators, the highest inter-orbital variability is found around periastron, and overall is stronger for the water-sensitive bands. While these differences in inter-orbital variability could provide a potential probe for distinguishing rotation rate, a more in-depth analysis of this effect would require simulation of a much larger number of orbits than what we have presented here. We leave such an analysis for future work.

4.2.3. Constructing Ratios of Light Curves

With all of the above features in mind, we construct "colors" by comparing the fluxes in two bands. Here we choose two pairs of bands: the bands at 7.7 and 10.0 μm, and the bands at
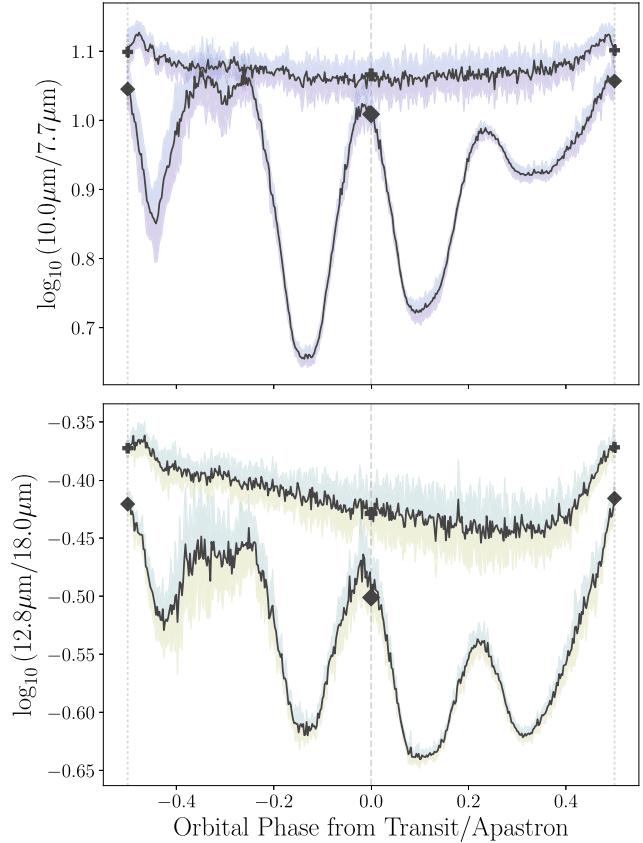
Figure 12. Ratios of a selection of the planet–star contrasts shown in the light curves of Figure 10, where the planet transits during apastron. Within each plot, the light curve with plus-sign markers shows Earth-like (fast) rotation, and the curve with diamond markers shows pseudo-synchronous (slow) rotation. The solid color lines are the averages over the final 10 orbits, and the surrounding shaded region represents the range of fluxes over the orbits. The choice of colors for these regions is purely to illustrate the fluxes used for each ratio.

12.8 and 18.0 μm (Figures 11 and 12). Each of these pairs compares one band where water has a strong absorption feature with another band in the water vapor window. For the first pair, which consist of shorter wavelengths, the longer-wavelength band is in the water vapor window while the shorter lies in the 6.3 μm vibrational–rotational absorption band of water vapor. The converse is true of the second pair of bands, which lie at longer wavelengths: the shorter-wavelength band is in the water vapor window and the longer one lies in the short-wavelength end of the pure rotational, far-infrared absorption band of water vapor. The behavior of these colors is discussed in greater detail in the Appendix.

For a transit–periastron viewing angle ($\varpi = 90°$) we see a consistent difference in the colors during or near periastron. The differences can be as high as 0.35 dex for both eccentricities. At $\varpi = 270°$, the peak difference between slow and fast rotators is not well aligned with periastron for $e = 0.3$, reaching a maximum notably prior to transit and having a smaller secondary maximum midway between transit and eclipse. At $e = 0.6$ and $\varpi = 270°$, the PSR period is short enough to allow a spike in each color near periastron for the slow rotator; large differences with the fast rotator thus occur about four times throughout the orbit consistent with the roughly 4:1 ratio of rotational to orbital periods. The $e = 0.6$ color curves exhibit some variations from orbit to orbit, but

one persistent feature is the set of secondary dips/peaks that correspond to the spin–orbit ratio.

Despite limiting our analysis of full-orbit photometry to two extreme cases of $\varpi = 90°$ and $270°$, it is relatively straightforward to predict the eclipse depths for the entire range of possible observing longitudes (Figure 13). The variations in eclipse depths with longitude in both cases show only minor variations relative to the ranges seen in Figures 11 and 12. Given this, it would be comparatively difficult to distinguish the scale of rotation from eclipse depths alone; therefore we also examine the night-side fluxes that one would observe during transit (Figure 14). Here we gain the advantage of the strong day–night water-induced contrasts seen in the slow-rotation cases. From these, we suggest that observations of day-side fluxes during/near eclipse, coupled with night-side fluxes during/near transit, could help discern these two cases.

The variations in eclipse depths with viewing geometry show a similar qualitative behavior to the phase curves with respect to rotation: the fast rotators exhibit a much weaker dependence on the observing angle than the slow rotators. This further suggests that, while maximizing the observing time would maximize the ability to discern between these cases, for a wide range of viewing geometries a pair of eclipse depths could hint at the broad timescale of rotation.
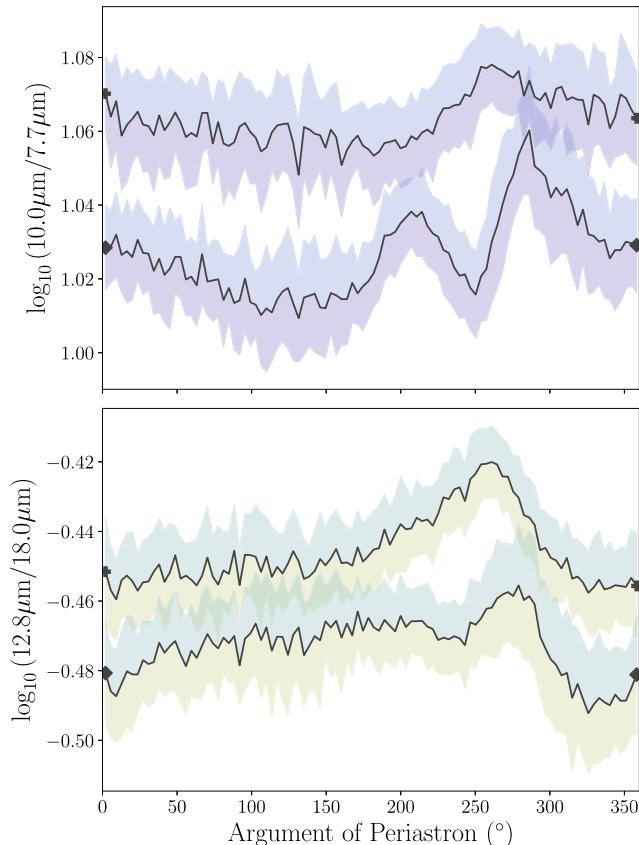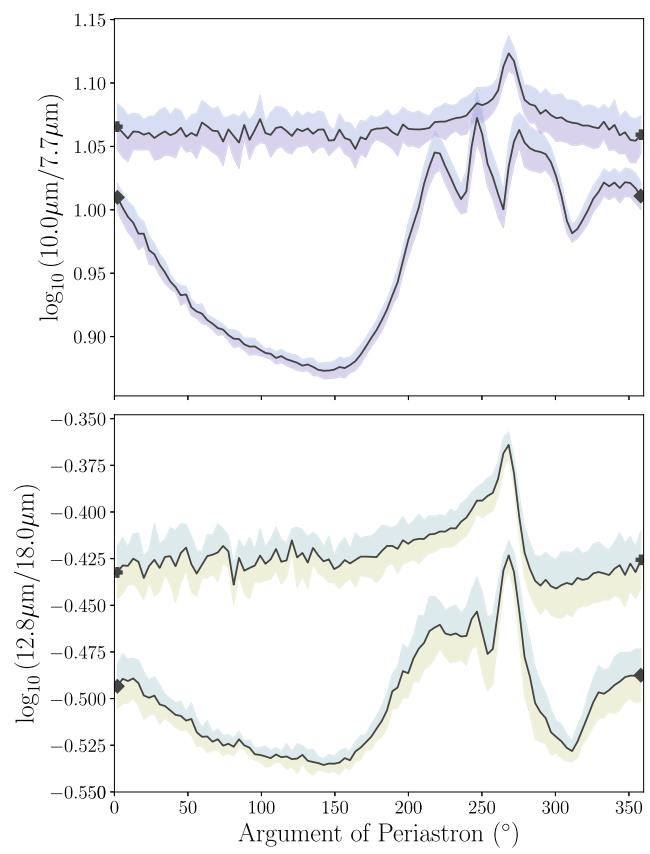
Figure 13. Predicted ratios of eclipse depths for the range of possible longitudes of periastron relative to an observer. The quantities plotted are identical to those in Figures 11 and 12. The solid colored lines are the averages over the final 10 orbits, and the surrounding shaded region represents the range of fluxes over the orbits. The choice of colors for these regions is purely to illustrate the fluxes used for each ratio.

5. Discussion

We showed that, for simulated ocean-covered planets on eccentric orbits, differences in the scale of rotation rate could be discernible from mid-infrared phase photometry of sufficient signal-to-noise ratio to detect a contrast of at least 1 ppm relative to the host star. We explicitly modeled two contrasting viewing geometries and demonstrate that differences of order ~0.3–0.4 dex in photometric contrast ratios would be distinguishable with a combination of broadband flux observations during transit and secondary eclipse. These differences are caused by the strong dependence of phase curve features, at particular wavelengths, on the concentration of upper-tropospheric water vapor. We have shown that, while any day–night contrasts in the temperature are restricted to layers near the planets' surfaces, day–night contrasts in atmospheric moisture concentration become very strong well into the upper atmosphere for rotations with periods comparable to the orbital period. These characteristic contrasts impart significant additional variations in those specific photometric bands that contain water absorption features, most notably in the MIRI band centered at 7.7 μm, but also broadly in the mid-infrared beyond approximately 20 μm.

Our results have used the instrumental responses for the upcoming *James Webb Space Telescope* to predict needed future mid-infrared sensitivity. The photometric precision required to discern the predicted variations is quite high, beyond what *JWST* will be capable of even with the most optimistic expectations. Looking forward to proposed space-based missions in this wavelength range, the Origins Space Telescope (OST) (Battersby et al. 2018) will have coverage in the mid-infrared with its Mid-Infrared Imager, Spectrometer, Coronagraph (MISC) instrument suite (Sakon et al. 2018). With an estimated precision of ~5 ppm in the range ~3–20 μm, OST is designed to have the potential to observe thermal phase variations of terrestrial planets (Fortney et al. 2018; Kataria 2018). Therefore, our findings point toward achieving these sorts of observations with a future generation of space observatories, perhaps first for planets in the HZs of smaller host stellar targets, such as K and M dwarfs.
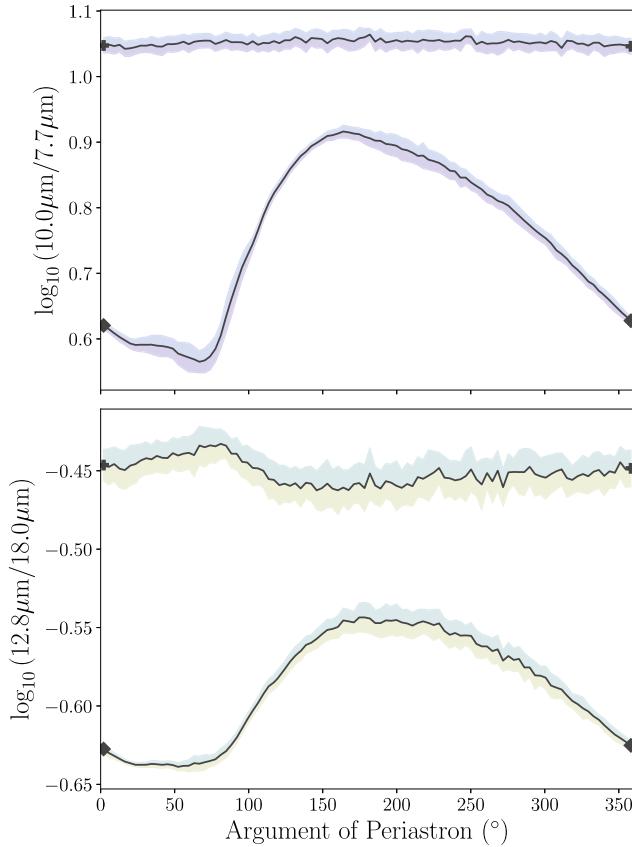
Works such as Cowan et al. (2012) have pointed out that a combination of thermal (IR) and reflected light (optical) observations would be necessary to fully characterize properties of exoplanets. As an exploration, we calculated the expected scale of phase variations in the optical and near-infrared by adopting the wide filter profiles of NIRCam on *JWST* (Space Telescope Science Institute 2017). The predicted scale is at best of order 10^{-10}. Therefore, while variations in reflected light hold interesting parallel physical observables, for the purposes and scope of this work our best case remains in the mid-infrared.

We also briefly explored the broad effect of ocean depth on our results, by re-running the $e = 0.3$ cases with ocean mixed layer depths of 10 m. The ice cover and cloud density increase slightly relative to the 50 m case at both extremes of the orbit,

$e = 0.3$ $e = 0.6$
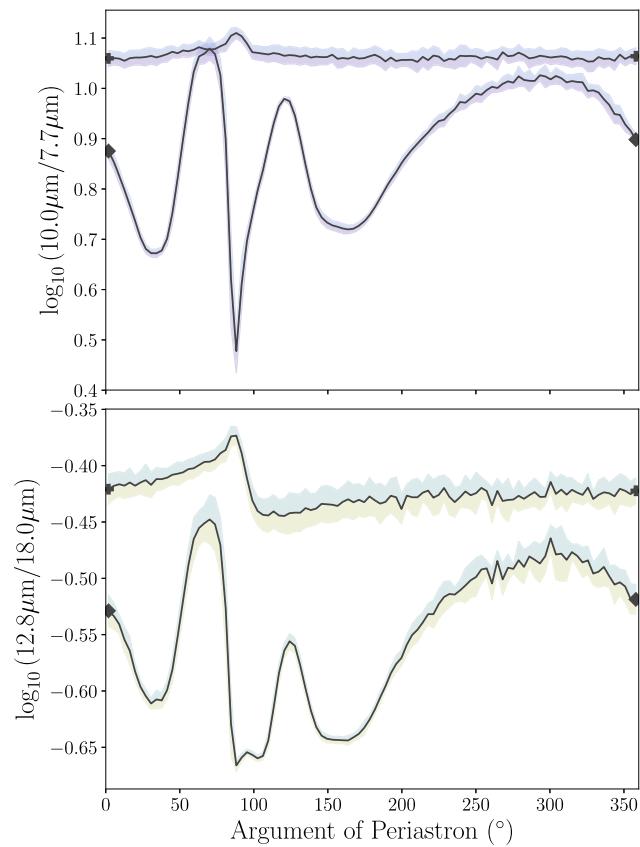
Figure 14. Predicted ratios of the observed night-side contrasts during transit for the range of possible longitudes of periastron relative to an observer. The quantities plotted are identical to those in Figures 11 and 12. The solid colored lines are the averages over the final 10 orbits, and the surrounding shaded region represents the range of fluxes over the orbits. The choice of colors for these regions is purely to illustrate the fluxes used for each ratio.

for both rotation periods. The fast-rotation curves do exhibit stronger amplitudes of phase variations compared with their deeper ocean counterparts, but this variation is still small compared with the average difference between rotation cases at fixed depth. From this we conclude that while the ocean depth has some effect on the observables, both the quality and quantity of differences are not significant enough to affect our conclusions.

While we have attempted to explore a constrained problem with as few added assumptions as possible, we acknowledge that we have not considered other dynamical and atmospheric effects that might cause large-amplitude variations in observables. In particular, we do not take into account the effects of tidal heating/dissipation, which could provide an additional forcing term to our systems. Additionally, the construction of transit and eclipse depths implies a narrow range of observed orbital inclinations, and we have assumed perfectly edge-on orbits in the construction of our predicted observables. This is a reflection of the detection bias inherent to transiting exoplanets; however, phase variations should persist even for non-transiting planets. We have also restricted ourselves to studying systems with solar-type host stars and mean instellations, even though studies such as Yang et al. (2013) predict that at instellations higher than Earth's, phase variations can effectively invert from the predictions for Earth-like instellation. Finally, we have assumed zero planetary obliquity; the interplay between the effects of the rotation and orbit in setting

the periodicities in heating in particular would be greatly sensitive to the orientation of the spin axis. In future work we will examine how these results change for a variety of conditions for temperate terrestrial exoplanets.

Appendix
Theoretical Estimates of Colors for Perfect Blackbodies

We constructed colors by taking the ratio of the planet–star contrast in one wavelength band to the planet–star contrast in a second wavelength band; we chose one band in a spectral

a) log(10.0/7.7)

b) log(12.8/18.0)
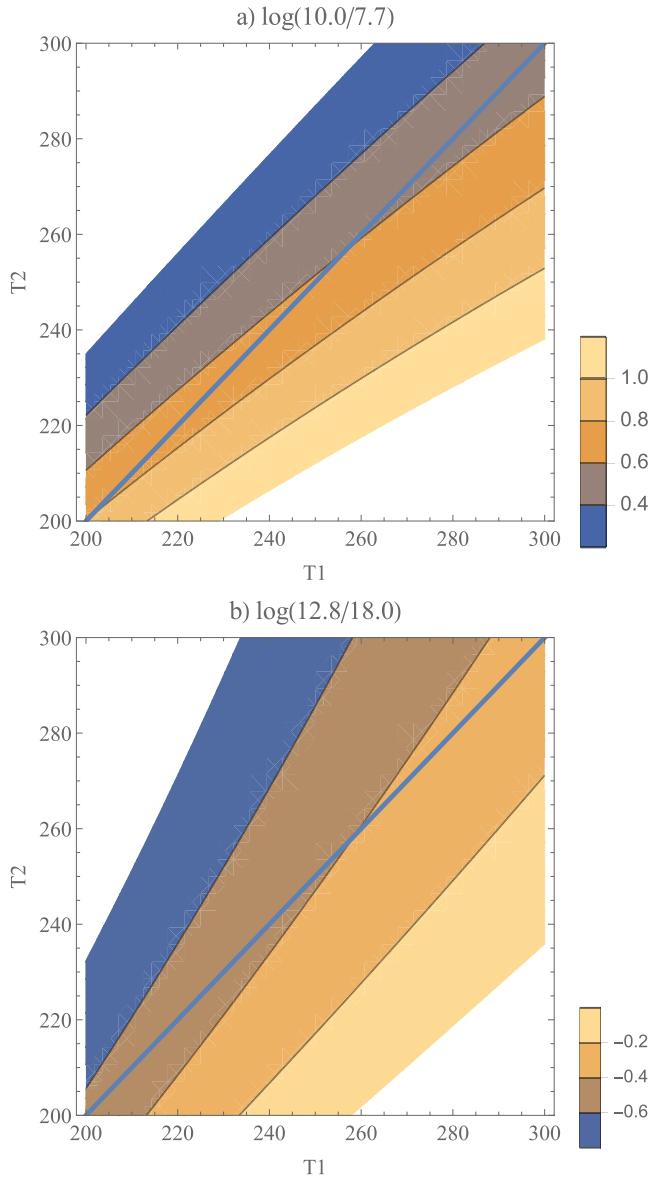
Figure 15. Theoretical "colors" for two perfect blackbodies at temperatures T_1 and T_2, in kelvin. As described in the text, these colors are constructed using the Planck function and assuming a blackbody star at 6000 K, and use wavelengths of (a) 10.0 and 7.7 μm, and (b) 12.8 and 18.0 μm. The shading represents the values of the theoretical color given in the title of each panel, and the blue line shows where $T_1 = T_2$.

region that is highly sensitive to water vapor absorption and the other in the water vapor window. Here we illustrate the utility of these colors by examining the idealized case where the emission in each band comes from a perfect blackbody.

In this idealized case, the planet–star contrast $P(\lambda, T)$ at wavelength λ and planetary temperature T is given in terms of the Planck function $B_\lambda(T)$,

$$P(\lambda, T) \propto \frac{B_\lambda(T)}{B_\lambda(T_\star)} \qquad (9)$$

where $T_\star$ is the emission temperature of the star, which we also approximate as a perfect blackbody. The quantity $P(\lambda, T)$ is a thermal idealization of an individual light curve (e.g., Figure 9). A color is then the ratio of the planet–star contrast at

wavelength λ_1 to that at wavelength λ_2,

$$C(\lambda_1, \lambda_2) = \frac{P(\lambda_1, T_1)}{P(\lambda_2, T_2)} = \frac{B_{\lambda_1}(T_1)B_{\lambda_2}(T_\star)}{B_{\lambda_2}(T_2)B_{\lambda_1}(T_\star)}. \qquad (10)$$

We assume that the emission at wavelength λ_i comes entirely from a layer of the atmosphere with temperature T_i, and we plot C as a function of T_1, T_2 for two particular combinations of wavelengths (Figure 15). For $(\lambda_1, \lambda_2) = (10.0\,\mu\text{m},\ 7.7\,\mu\text{m})$, lines of constant C are slightly less steep than the one-to-one line. For a uniform warming of T_1 and T_2, an increase of 100 K is thus required to produce a decrease in C of about 0.2 to 0.3 dex, while the same change in C can be achieved by a differential warming in those temperatures of only 10–15 K. Similar behavior is exhibited for $(\lambda_1, \lambda_2) = (12.8\,\mu\text{m}, 18.0\,\mu\text{m})$, except that, because of the reverse ordering of wavelengths, a uniform warming of 100 K produces an increase of about 0.2 dex, while that same increase can be achieved by a differential warming of 10–15 K. Thus, C is relatively insensitive to a uniform planetary warming or cooling, and is about an order of magnitude more sensitive to differential changes in the emission levels of the two wavelengths chosen for C. For example, if one wavelength for C is located in the water vapor window and the other in a spectral band with strong water vapor absorption, we would expect to see a large change in C as we move from viewing a dry side of the planet (where T_1 and T_2 are nearly the same) to viewing a humid side. The changes in emission due to the water-specific features are able to dominate the color variations over the orbit-induced thermal color variations.

ORCID iDs

Arthur D. Adams https://orcid.org/0000-0002-7139-3695
William R. Boos https://orcid.org/0000-0001-9076-3551
Eric T. Wolf https://orcid.org/0000-0002-7188-1648

References

Adams, A. D., & Kane, S. R. 2016, AJ, 152, 4
Adams, A. D., & Laughlin, G. 2018, AJ, 156, 28
Astropy Collaboration, Robitaille, T., Tollerud, E., et al. 2013, A&A, 558, A33
Bardeen, C. G., Garcia, R. R., Toon, O. B., & Conley, A. J. 2017, PNAS, 114, E7415
Barnes, J., Haberle, R., Pollack, J., Lee, H., & Schaeffer, J. 1996, JGR, 101, 12753
Barnes, J., Pollack, J., Haberle, R., et al. 1993, JGR, 98, 3125
Barnes, J. R., & Haberle, R. M. 1996, JAtS, 53, 3143
Barnes, R., Raymond, S., Jackson, B., & Greenberg, R. 2008, AsBio, 8, 557
Battersby, C., Armus, L., Bergin, E., et al. 2018, NatAs, 2, 596
Bengtsson, L., Bonnet, R.-M., Grinspoon, D., et al. 2013, Towards Understanding the Climate of Venus (New York: Springer)
Bitz, C. M., Shell, K. M., Gent, P. R., et al. 2012, JCli, 25, 3053
Bolmont, E., Libert, A.-S., Leconte, J., & Selsis, F. 2016, A&A, 591, A106
Brent, R. P. 1973, Algorithms for Minimization without Derivatives (Englewood Cliffs, NJ: Prentice-Hall)
Chiang, J. C. H., & Bitz, C. M. 2005, ClDy, 25, 477
Cowan, N., & Agol, E. 2011, ApJ, 726, 82
Cowan, N. B., Voigt, A., & Abbot, D. S. 2012, ApJ, 757, 80
Cullum, J., Stevens, D., & Joshi, M. 2014, AsBio, 14, 645
Deitrick, R., Barnes, R., Bitz, C., et al. 2018, AJ, 155, 266
de Wit, J., Lewis, N. K., Langton, J., et al. 2016, ApJL, 820, L33
Forget, F., Hourdin, F., Fournier, R., et al. 1999, JGR, 104, 24155
Forget, F., Wordsworth, R., Millour, E., et al. 2013, Icar, 222, 81
Fortney, J., Kataria, T., Stevenson, K., et al. 2018, arXiv:1803.07730
Georgakarakos, N., Dobbs-Dixon, I., & Way, M. J. 2016, MNRAS, 461, 1512
Glasse, A., Rieke, G., Bauwens, E., et al. 2015, PASP, 127, 686

Goldreich, P., & Soter, S. 1966, Icar, 5, 375
Haberle, R., Pollack, J., Barnes, J., et al. 1993, JGR, 98, 3093
Hack, J. J. 1994, JGR, 99, 5551
Hunke, E. C., & Lipscomb, W. H. 2008, CICE: The Los Alamos Sea Ice Model, Documentation and Software User's Manual, Version 4.0, Tech. Rep. LA-CC-06-012, Los Alamos National Laboratory, Los Alamos, New Mexico
Hunter, J. D. 2007, CSE, 9, 90
Hut, P. 1981, A&A, 99, 126
Jones, E., Oliphant, T., Peterson, P., et al. 2001, SciPy: Open source scientific tools for Python, http://www.scipy.org/
Joshi, M., Haberle, R., & Reynolds, R. 1997, Icar, 129, 450
Kasting, J., Whitmire, D., & Reynolds, R. 1993, Icar, 101, 108
Kataria, T. 2018, in COSPAR Meeting 42, XLII COSPAR Sci. Assem. (Pasadena, CA: COSPAR), E4.1
Kataria, T., Showman, A., Lewis, N., et al. 2013, ApJ, 767, 76
Kluyver, T., Ragan-Kelley, B., Perez, F., et al. 2016, Jupyter Notebooks – A Publishing Format for Reproducible Computational Workflows (Amsterdam: IOS Press)
Kopparapu, R., Ramirez, R., Kasting, J., et al. 2013, ApJ, 765, 131
Kopparapu, R., Ramirez, R., SchottelKotte, J., et al. 2014, ApJL, 787, L29
Kopparapu, R., Wolf, E. T., Arney, G., et al. 2017, ApJ, 845, 5
Kovesi, P. 2015, arXiv:1509.03700
Kozai, Y. 1962, AJ, 67, 591
Kreidberg, L. 2018, in Handbook of Exoplanets, ed. H. Deeg & J. Belmonte (Cham: Springer International), 1
Langton, J., & Laughlin, G. 2008, ApJ, 674, 1106
Lebonnois, S., Hourdin, F., Eymet, V., et al. 2010, JGR, 115, E06006
Leconte, J., Forget, F., Charnay, B., et al. 2013, A&A, 554, A69
Lewis, N., Parmentier, V., Kataria, T., et al. 2017, arXiv:1706.00466
Lidov, M. 1962, P&SS, 9, 719
Lin, S., & Rood, R. 1997, QJRMS, 123, 2477
Lin, S.-J., & Rood, R. 1996, MWRv, 124, 2046
Linsenmeier, M., Pascale, S., & Lucarini, V. 2015, P&SS, 105, 43
Makarov, V. V., & Efroimsky, M. 2013, ApJ, 764, 27
Merlis, T., & Schneider, T. 2010, JAMES, 2, 13
Murray, C., & Dermott, S. 1999, Solar System Dynamics (New York: Cambridge Univ. Press)
Neale, R. B., Chen, C.-C., & Gettelman, A. 2010, Description of the NCAR Community Atmosphere Model (CAM 5.0), Tech. Rep., TN-485+STR
O'Dell, C. W., Wentz, F. J., & Bennartz, R. 2008, JCli, 21, 1721
O'Gorman, P., & Schneider, T. 2008, JCli, 21, 3815
Parmentier, V., & Crossfield, I. J. M. 2018, in Handbook of Exoplanets, ed. H. Deeg & J. Belmonte (Cham: Springer International), 1

Paynter, D. J., & Ramaswamy, V. 2011, JGR, 116, D20302
Pierrehumbert, R. T., & Hammond, M. 2019, AnRFM, 51, 275
Pincus, R., Barker, H. W., & Morcrette, J.-J. 2003, JGRD, 108, 4376
Ramirez, R. 2018, Geosc, 8, 280
Ramirez, R., & Kaltenegger, L. 2016, ApJ, 823, 1
Rasch, P. J., & Kristjánsson, J. E. 1998, JCli, 11, 1587
Raymond, D. J., & Blyth, A. M. 1986, JAtS, 43, 2708
Raymond, D. J., & Blyth, A. M. 1992, JAtS, 49, 1968
Rieke, G., Wright, G., Böker, T., et al. 2015, PASP, 127, 584
Rossow, W. 1983, JAtS, 40, 273
Sakon, I., Roellig, T. L., Ennico-Smith, K., et al. 2018, Proc. SPIE, 10698, 1069817
Schneider, T. 2006, AREPS, 34, 655
Selsis, F., Maurin, A. S., Hersant, F., et al. 2013, A&A, 555, A51
Shields, A., Bitz, C., Meadows, V., Joshi, M., & Robinson, T. 2014, ApJL, 785, L9
Shields, A., Meadows, V., Bitz, C., et al. 2013, AsBio, 13, 715
Shields, A. L. A., Barnes, R., Agol, E., et al. 2016, AsBio, 16, 443
Showman, A., Cho, J.-K., & Menou, K. 2010, in Exoplanets, ed. S. Seager (Tucson, AZ: Univ. Arizona Press), 471
Showman, A., & Guillot, T. 2002, A&A, 385, 166
Space Telescope Science Institute 2017, NIRCam Imaging (Baltimore, MD: JWST User Documentation), https://jwst-docs.stsci.edu/display/JTI/NIRCam+Imaging
Space Telescope Science Institute 2018, MIRI Imaging (Baltimore, MD: JWST User Documentation), https://jwst-docs.stsci.edu/display/JTI/MIRI+Overview
Spiegel, D., Raymond, S., Dressing, C., Scharf, C., & Mitchell, J. 2010, ApJ, 721, 1308
Staníček, P. 2018, Paletton, The Color Scheme Designer, http://paletton.com/
Toon, O. B., McKay, C. P., Ackerman, T. P., & Santhanam, K. 1989, JGR, 94, 16287
van der Walt, S., Colbert, S. C., & Varoquaux, G. 2011, CSE, 13, 22
Way, M. J., Del Genio, A. D., Aleinov, I., et al. 2018, ApJS, 239, 24
Way, M. J., & Georgakarakos, N. 2016, ApJL, 835, 1
Werner, M., Roellig, T., Low, F., et al. 2004, ApJS, 154, 1
Williams, D. M., & Pollard, D. 2002, IJAsB, 1, 61
Wolf, E., & Toon, O. 2013, AsBio, 13, 656
Wolf, E., & Toon, O. 2014, GeoRL, 41, 167
Wolf, E., & Toon, O. 2015, JGRD, 120, 5775
Wright, G., Wright, D., Goodson, G., et al. 2015, PASP, 127, 595
Yang, J., Cowan, N. B. N., & Abbot, D. D. S. 2013, ApJL, 771, L45
Zalucha, A., Plumb, R., & Wilson, R. 2010, JAtS, 67, 673
Zhang, G. J., & McFarlane, N. A. 1995, JGR, 100, 1417